2D CFD simulations of flow and reaction during carbon dioxide methanation: A spatially resolved channel plate reactor study

Chemical Engineering Science 282 (2023) 119235

Contents lists available at ScienceDirect

Chemical Engineering Science

journal homepage: www.elsevier.com/locate/ces

2D CFD simulations of flow and reaction during carbon dioxide methanation: A spatially resolved channel plate reactor study

Toyin Omojola *, Lars Davidson

Division of Fluid Dynamics, Department of Mechanics and Maritime Sciences, Chalmers University of Technology, Gothenburg, SE 412 – 96, Sweden

ARTICLE INFO

Keywords:
Carbon dioxide methanation
Power-to-gas
Spatially resolved study
Channel plate reactor
CFD simulation

ABSTRACT

Carbon dioxide methanation is a way of storing excess electrical energy as grid compatible gas. Spatially resolved channel plate reactor experiments were used to validate competing reactor (1D, $2D_{x\text{-}z}$) models. Parallel exothermic carbon dioxide methanation and endothermic reverse water gas shift reactions were considered. The kinetic model, where the rate determining step is between an oxygenated complex (HCOO*) and an active site (*), was used in $2D_{x\text{-}z}$ CFD simulations for six laminar inflow conditions and variations in pressure, temperature, H_2/CO_2 ratio, methane, and steam co-feeds. The performance is improved by decreasing flowrate, and increasing H_2/CO_2 ratio, pressure, and temperature. Co-feeding methane has a negligible effect on reactor performance. However, co-feeding steam significantly reduces performance. At relatively high conversions, differential rates are obtained. This is due to the negligible dependence of the rate of carbon dioxide conversion with the equilibrium term of the reverse water gas shift reaction. With these studies, a link between the reaction mechanism and reactor performance is established at conditions relevant to power-to-gas applications.

1. Introduction

The European Council projects that a greenhouse gas emissions reduction target of 50% must be achieved by 2030 to attain the objective of becoming climate neutral by 2050. A goal of 32% renewable energy was proposed to constitute the EU's overall energy mix by 2030 (European-Commission, 2021). Renewable energy sources, such as wind and solar energy, which have a significant role to play, fluctuate and have to be balanced for electric grid purposes (Götz et al., 2016). Consequently, electricity storage and reserve production capacity are required. The power-to-gas process converts surplus power into grid compatible gas through a two-step process: (a) hydrogen production by water electrolysis, and (b) hydrogen conversion with an external carbon monoxide or carbon dioxide source to methane *via* methanation (Götz et al., 2016; Wulf et al., 2018). Carbon dioxide methanation allows for the conversion of greenhouse gases to substitute natural gas which can be stored, introduced into the gas distribution grid, or used as a motor fuel.

Various reactors have been used to investigate the kinetics of carbon dioxide methanation including differential (Weatherbee and Bartholomew, 1982; Inoue and Funakoshi, 1984), integral (Kai et al., 1988; Garbis et al., 2019; Miguel et al., 2018), and spatially resolved reactors (Froment et al., 2011; Bosco and Vogel, 2006; Kopyscinski et al., 2010; Hernandez Lalinde et al., 2018; Lalinde et al., 2019; Hernandez Lalinde, 2020; Surendran, 2022). Other reactor concepts including foam reactors, microchannel reactors, and milli structured reactors have been used (Bengaouer et al., 2018; Raghu and Kaisare, 2022; Engelbrecht et al., 2020; Engelbrecht et al., 2017; Danilov et al., 2022; Chandraker et al., 2022). The differential reactors are limited to conversions of less than 5%. Integral reactors allow higher conversions but lead to axial and radial concentration gradients which make kinetic measurements difficult due to the unexplored spatial variation in rates. Spatially resolved reactors (Serrer et al., 2021) allow the measurement of these concentration and temperature gradients and thus provide an elucidation of the kinetic profiles. Catalytic plate (channel) reactors are a configuration of spatially resolved reactors that possess advantages over fixed bed, fluidised bed, coated metal foam reactors due to their high surface area-to-volume ratio and their excellent heat transfer along with a small pressure drop. Such channel reactors (Hernandez Lalinde, 2020; Engelbrecht et al., 2017) can be made optically accessible by enabling temperature measurement using infra-red thermography and a movable stainless-steel capillary that allows for the acquisition of spatial concentration profiles. Conventionally, mass transfer or kinetic control during kinetic experiments is determined at the reactor exit in a fixed bed reactor.

* Corresponding author.
E-mail address: toyin.omojola@bath.edu (T. Omojola).

https://doi.org/10.1016/j.ces.2023.119235
Received 15 March 2023; Received in revised form 10 August 2023; Accepted 29 August 2023
Available online 31 August 2023

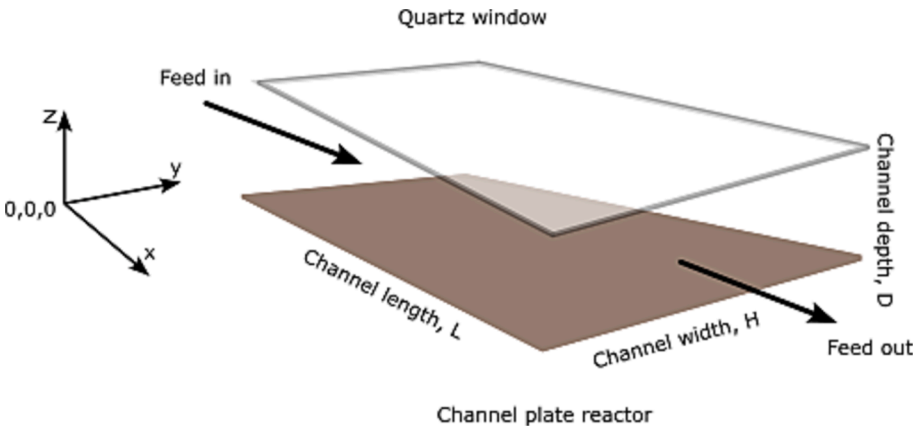

Fig. 1. A schematic of a channel plate reactor for carbon dioxide methanation. The boundary conditions for the 1D and $2D_{x\text{-}z}$ models can be found in Tables 1 and 2. The dimension of the channel plate reactor is 0.054 m by 0.04 m.

Table 1
Boundary conditions for $2D_{x\text{-}z}$ model.

	U	W	Specie, except argon	Argon
Left	$U\|_{x=0} = U_\infty$	$W\|_{x=0} = 0$	$w_i\|_{x=0} = w_{i,feed}$	$w_{Ar}\|_{x=0} = w_{Ar,feed}$
Right	$\left.\frac{dU}{dx}\right\|_{x=L} = 0$	$\left.\frac{dW}{dx}\right\|_{x=L} = 0$	$\left.\frac{dw_i}{dy}\right\|_{x=L} = 0$	$\left.\frac{dw_{Ar}}{dy}\right\|_{x=L} = 0$
Bottom	$\left.\frac{dU}{dz}\right\|_{z=0} = 0$	$W\|_{z=0} = 0$	$\left.\frac{dw_i}{dz}\right\|_{z=0} = 0$	$w_{Ar}\|_{z=0} = w_{Ar,feed}$
Top	$\left.\frac{dU}{dz}\right\|_{z=D} = 0$	$W\|_{z=D} = 0$	$\left.\frac{dw_i}{dz}\right\|_{z=D} = 0$	$w_{Ar}\|_{z=D} = w_{Ar,feed}$

Table 2
Boundary conditions for the 1D model.

	U	Species, except argon	Argon
Left	$U\|_{x=0} = U_\infty$	$w_i\|_{x=0} = w_{i,feed}$	$w_{Ar}\|_{x=0} = w_{Ar,feed}$
Right	$\left.\frac{dU}{dx}\right\|_{x=L} = 0$	$\left.\frac{dw_i}{dx}\right\|_{x=L} = 0$	$\left.\frac{dw_{Ar}}{dy}\right\|_{x=L} = 0$

Table 3
Kinetic parameters for carbon dioxide methanation and RWGS (Hernandez Lalinde, 2020).

Parameter	Units	Values
$k_{CO2,meth}$ (T_{ref})	mol kg_{cat}^{-1} s^{-1} $bar^{-0.5}$	1.82 ± 0.64
$E_{A,CO2\ meth}$	kJ mol^{-1}	22.9 ± 23.2
k_{RWGS} (T_{ref})	mol kg_{cat}^{-1} s^{-1} bar^{-1}	0.11 ± 0.01
$E_{A,RWGS}$	kJ mol^{-1}	179.1 ± 7.4
K_{HCOO} (T_{ref})	$bar^{-0.5}$	0.70 ± 0.21
ΔH_{HCOO}	kJ mol^{-1}	96.3 ± 19.6
K_{H2} (T_{ref})	bar	3.25 ± 2.30
ΔH_{H2}	kJ mol^{-1}	−18.9 ± 66.9
K_{OH} (T_{ref})	bar^{-1}	2.65 ± 0.64
ΔH_{OH}	kJ mol^{-1}	51.5 ± 23.3
K_β (T_{ref})	–	4.44 ± 0.13
ΔH_β	kJ mol^{-1}	−20.4 ± 2.1

Since the concentration gradients are elucidated using a spatially resolved channel reactor, an opportunity to determine the switch between kinetic and mass transfer control along the channel with process parameters is presented.

Several reactor models have been used to simulate various reactor concepts. One-dimensional (1D) models (Hernandez Lalinde, 2020; Engelbrecht et al., 2017; Farsi et al., 2021; Garbarino et al., 2020; Sun et al., 2017; Ngo, 2020) have been used for a heat exchanger reactor, packed bed reactor, fixed bed reactor and a bubbling fluidised bed reactor. One-dimensional models are constructed with respect to the axial length of the fixed bed reactor. Two-dimensional (2D) models (Fache and Marias, 2020; Schlereth et al., 2015) have been used to investigate methanation reactions in metallic honeycomb reactors and fixed bed reactors. Two-dimensional models are constructed with respect to the axial length and radius of the fixed bed reactor. Three-dimensional (3D) models (Surendran, 2022; Raghu and Kaisare, 2022; Engelbrecht et al., 2017; Vidal Vázquez et al., 2018; Pérez et al., 2019; Raghu and Kaisare, 2019; Türks et al., 2017) have been used to investigate multichannel reactor, microchannel reactors, monolithic reactors, and fixed bed reactors. Three-dimensional models cover all space dimensions in the reactor. Although various reactor models have been used for different reactor concepts, there are limited studies on the influence of flowrate on the axial and transverse concentration of species in the reactor. Such studies can be determined by 2D reactor models. Moreover, there are limited or no 2D reactor models applied to channel reactors which provide spatial resolution on concentration and/or temperature gradients during kinetic studies for carbon dioxide methanation.

Nickel, ruthenium, and rhodium-based catalysts have been used to investigate the kinetics of carbon dioxide methanation in chemical reactors (Weatherbee and Bartholomew, 1982; Chiang and Hopper, 1983; Weatherbee and Bartholomew, 1981; Burger et al., 2021; Schmider et al., 2021; Alarcón et al., 2021; Falbo et al., 2018). Of these, nickel-based catalysts are the most widely used due to their low cost and high abundance. During carbon dioxide methanation, two major reactions occur. These include carbon dioxide methanation (r_1) and the reverse water gas shift reaction (r_2). Over nickel catalysts, in order to accurately describe the kinetics of carbon dioxide methanation, the competing reverse water gas shift reaction should be included in mechanistic and performance studies (Hernandez Lalinde, 2020). Carbon monoxide methanation (Kopyscinski et al., 2010) reaction could be included, however, the concentrations of carbon monoxide produced during carbon dioxide methanation in channel reactors are too little to

Table 4
Decomposition of the rate of methanation, and the rate of the reverse water gas shift reaction into the (rate constant × driving force), equilibrium term, and adsorption term.

	(rate constant × driving force)	*Equilibrium term*	*Adsorption term*
r_1, Methanation	$k_{CO2,meth} \bullet K_{HCOO} \bullet p_{CO2} \bullet K_{H2}^{0.5} p_{H2}^{0.5}$	$1-\left(\frac{p_{H2O}^2 \bullet p_{CH4}}{p_{H2}^4 \bullet p_{CO2} \bullet K_{eqM}}\right)$	$\frac{1}{\left(1+K_{HCOO} \bullet p_{CO2} \bullet K_{H2}^{0.5} \bullet p_{H2}^{0.5}+\sqrt{K_{H2} p_{H2}}+K_{OH}\frac{p_{H2O}}{\sqrt{p_{H2}}}\right)^2}$
r_2, RWGS	$k_{RWGS} \bullet p_{CO2} \bullet K_{H2}^{0.5} \bullet p_{H2}^{0.5}$	$1-\left(K_\beta \frac{p_{CO} \bullet p_{H2O}}{p_{H2} \bullet p_{CO2} \bullet K_{eqRWGS}}\right)$	$\frac{1}{\left(1+K_{HCOO} \bullet p_{CO2} \bullet K_{H2}^{0.5} \bullet p_{H2}^{0.5}+\sqrt{K_{H2} p_{H2}}+K_{OH}\frac{p_{H2O}}{\sqrt{p_{H2}}}\right)^2}$

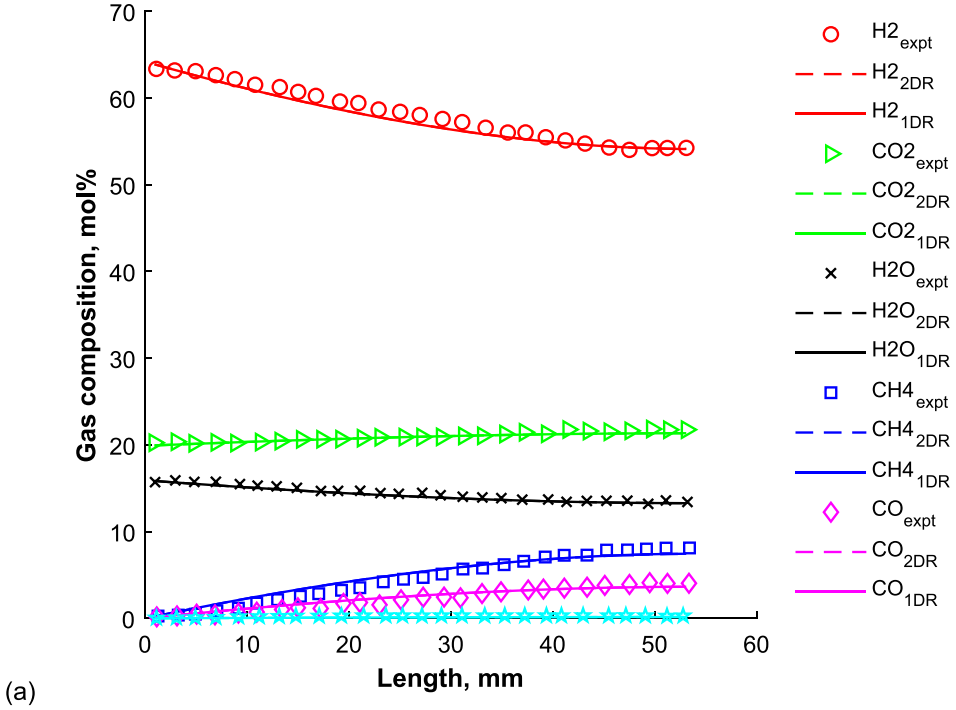

(a)

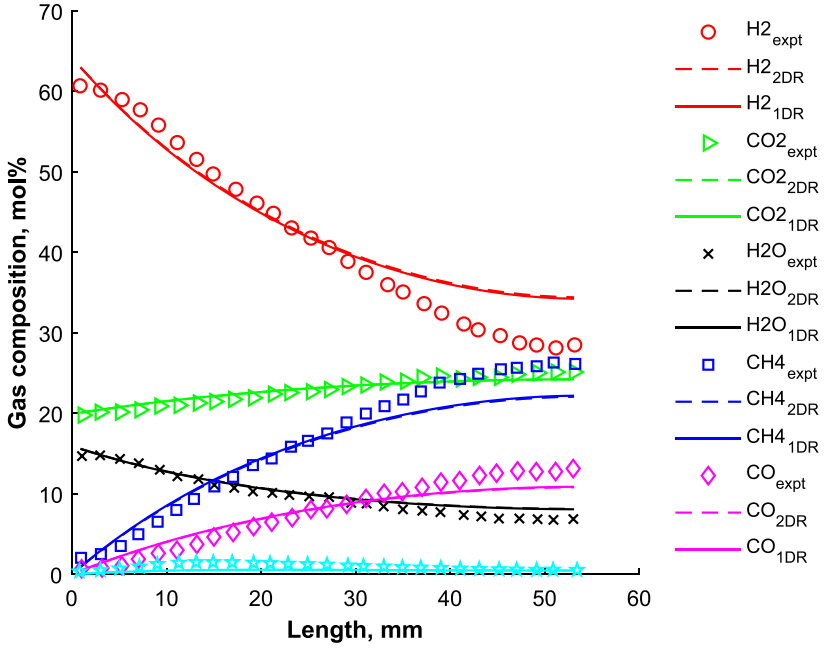

(b)

Fig. 2. Concentration profiles obtained at 100 NmL min^{-1} with an inlet feed of 64 mol% hydrogen, 16 mol% carbon dioxide, and 20 mol% argon at (a) 320 °C and (b) 400 °C.

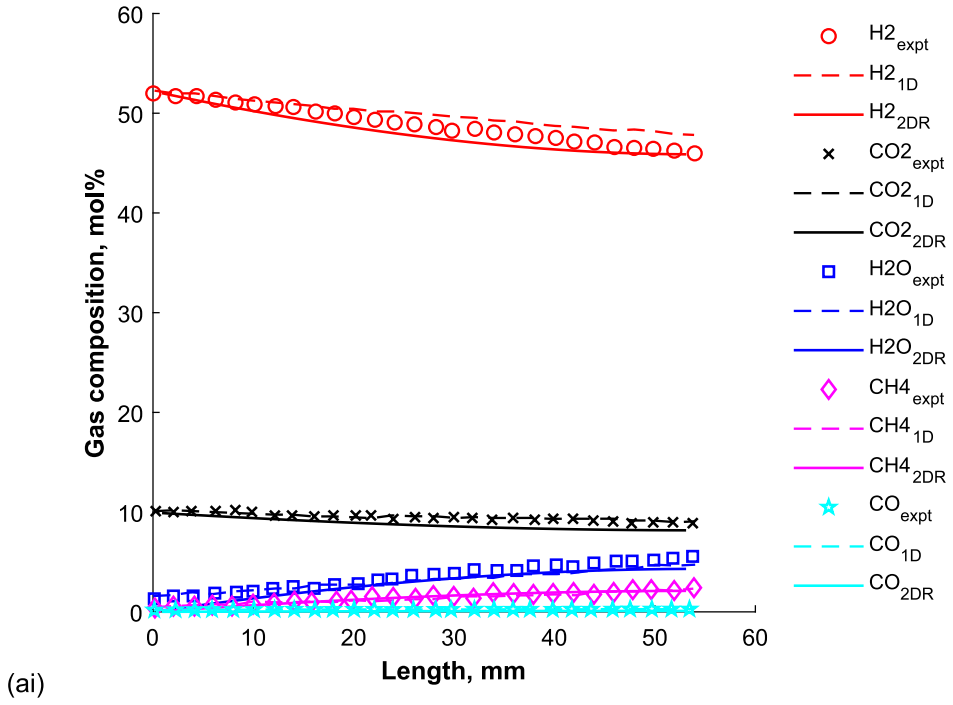

(ai)

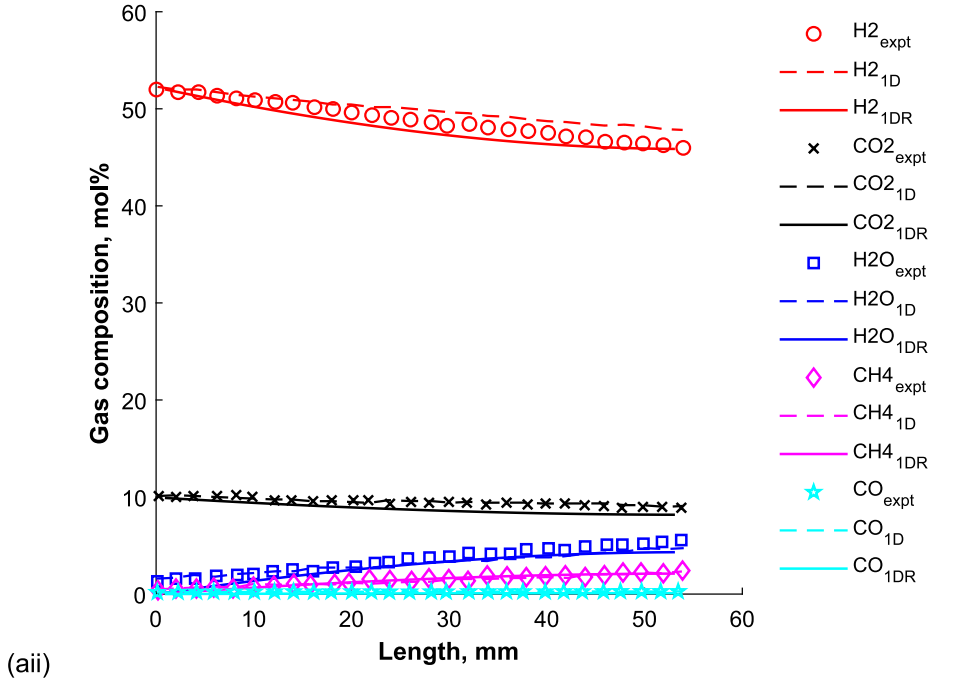

(aii)

Fig. 3. Comparison of channel reactor experimental data with a 1D two-phase model (1D), 1D CFD (1DR) simulation and 2D CFD (2DR) simulation at (a) 100 NmL min^{-1}, 320 °C and 1.2 bar, (b) 100 NmL min^{-1}, 380 °C and 1.2 bar.

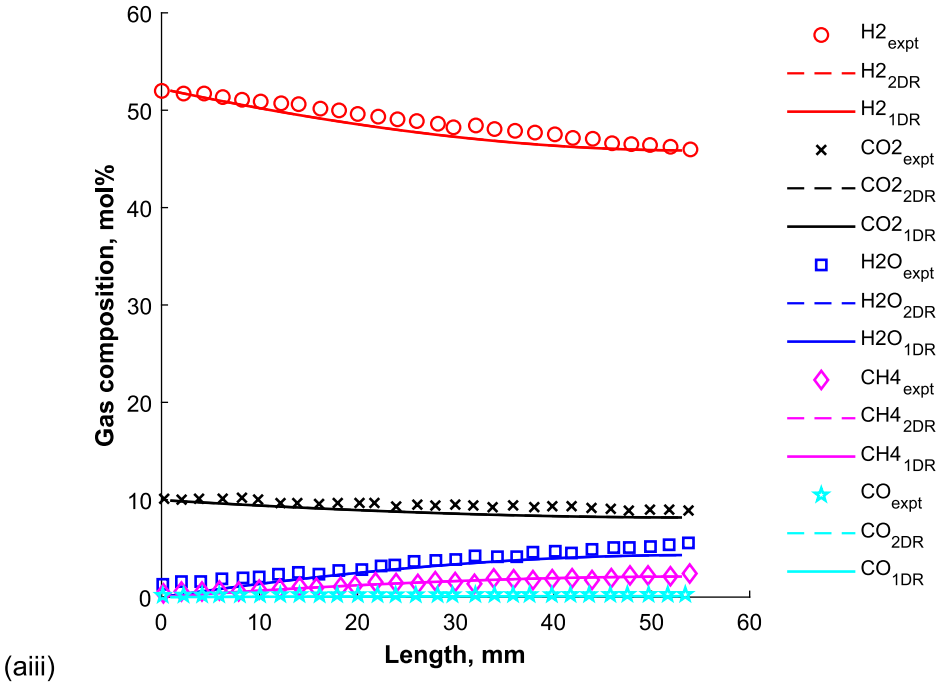

(aiii)

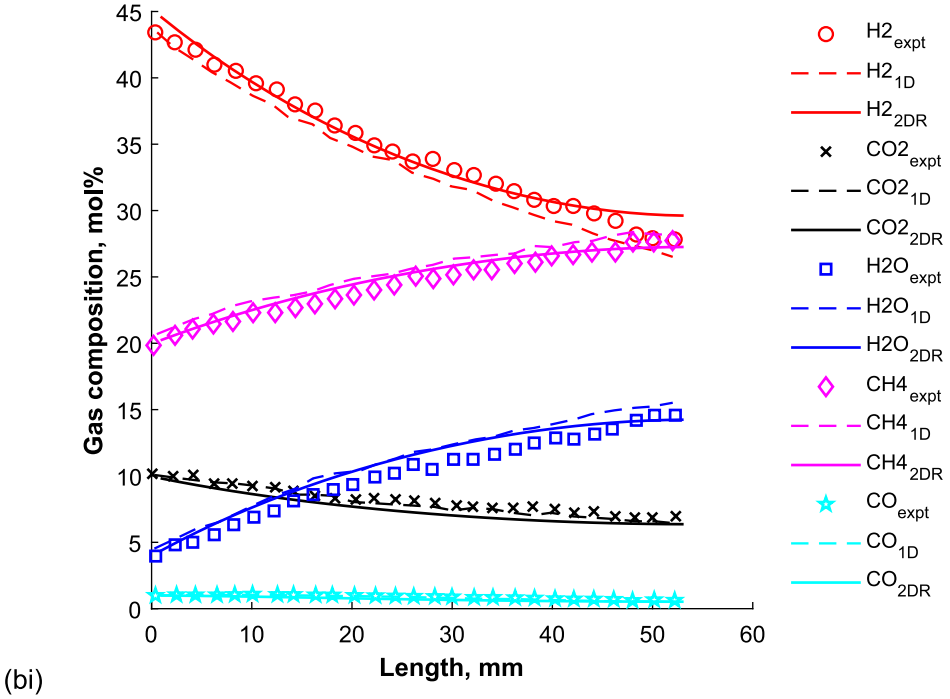

(bi)

Fig. 3. (*continued*).

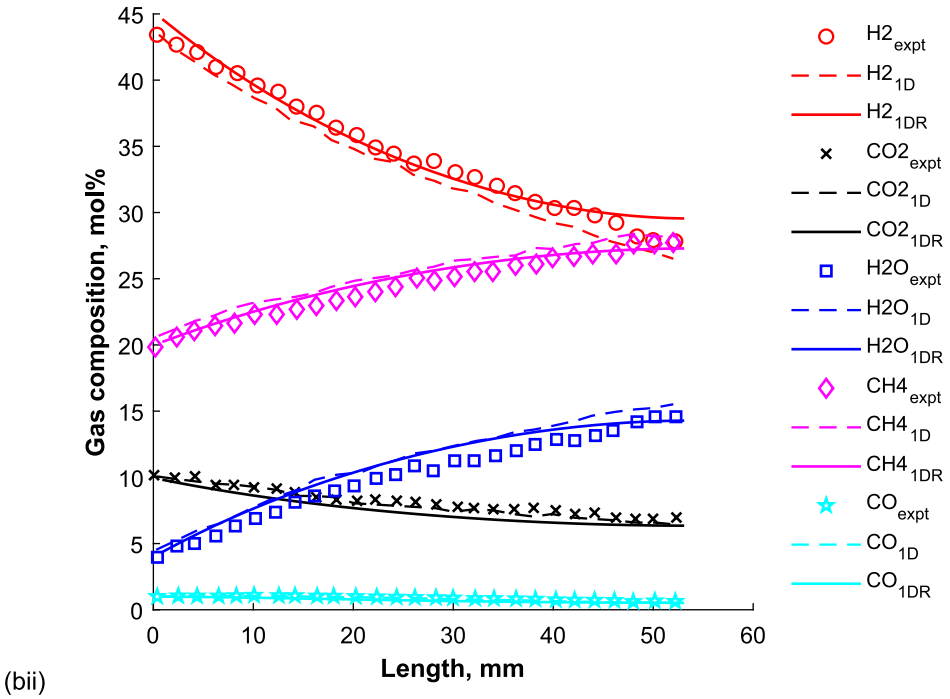

(bii)

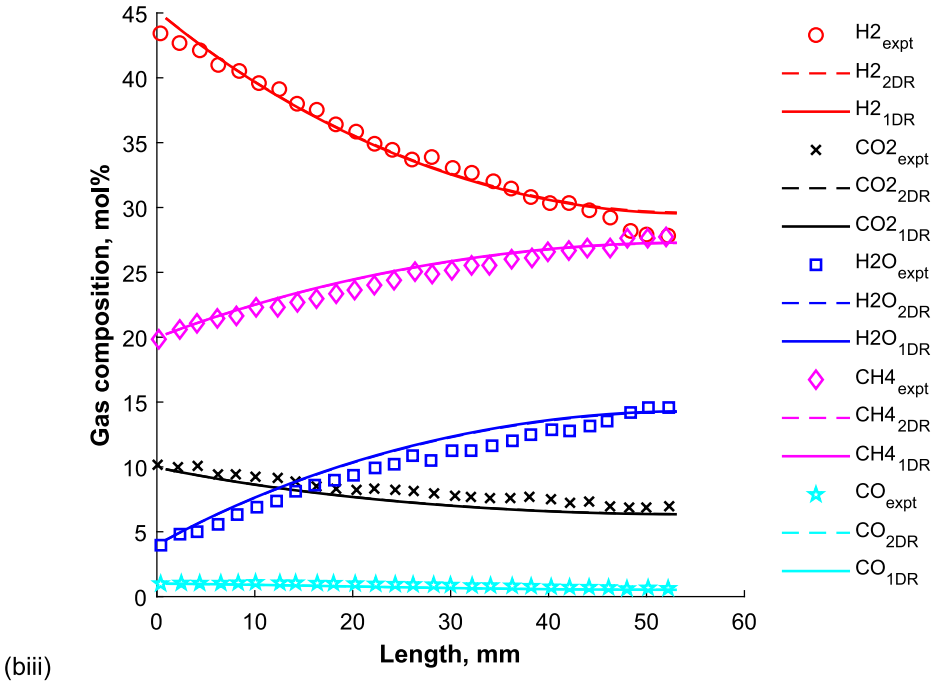

(biii)

Fig. 3. (*continued*).

be consequential. Nonetheless, Hinrichsen and co-workers (Burger et al., 2021) investigated the kinetics and competitive adsorption of carbon monoxide and carbon dioxide in the feed gas so as to simulate CO_x supply from the gasification of coal or biomass, for power-to-gas applications.

$r_1: \ CO_2 + 4H_2 \leftrightarrow CH_4 + 2H_2O \quad \Delta H_R^0 = -165 kJmol^{-1}$

$r_2: \ CO_2 + H_2 \leftrightarrow CO + H_2O \quad \Delta H_R^0 = 41 kJmol^{-1}$

Recent kinetic models obtained with channel reactors attempt to describe carbon dioxide methanation and competing reverse water gas shift reaction through Langmuir-Hinshelwood Hougen Watson (LHHW) kinetic rate expressions (Kopyscinski et al., 2010; Hernandez Lalinde, 2020). The kinetics of carbon dioxide methanation under steady state has also been described with a simple power law expression (Chiang and Hopper, 1983; Van Herwijnen et al., 1973) while later models used a LHHW kinetic model which compare different rate expressions depending on the rate determining step. Kopyscinski and co-workers

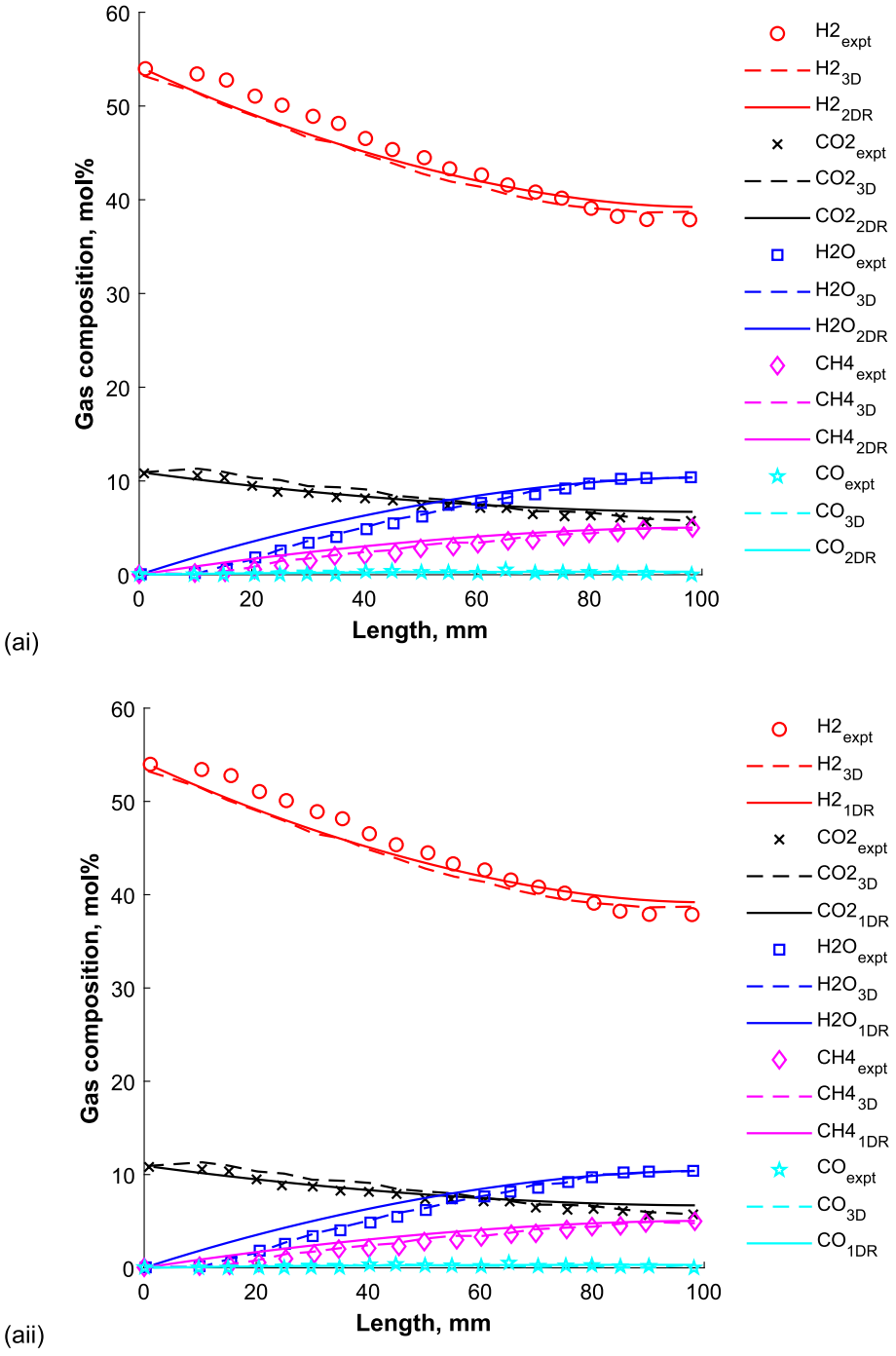

Fig. 4. Comparison of channel reactor experimental data with a 3D CFD model, 1D CFD simulation, and $2D_{x\text{-}z}$ CFD simulation at 150 NmL min^{-1}, 360 °C and 1.2 bar.

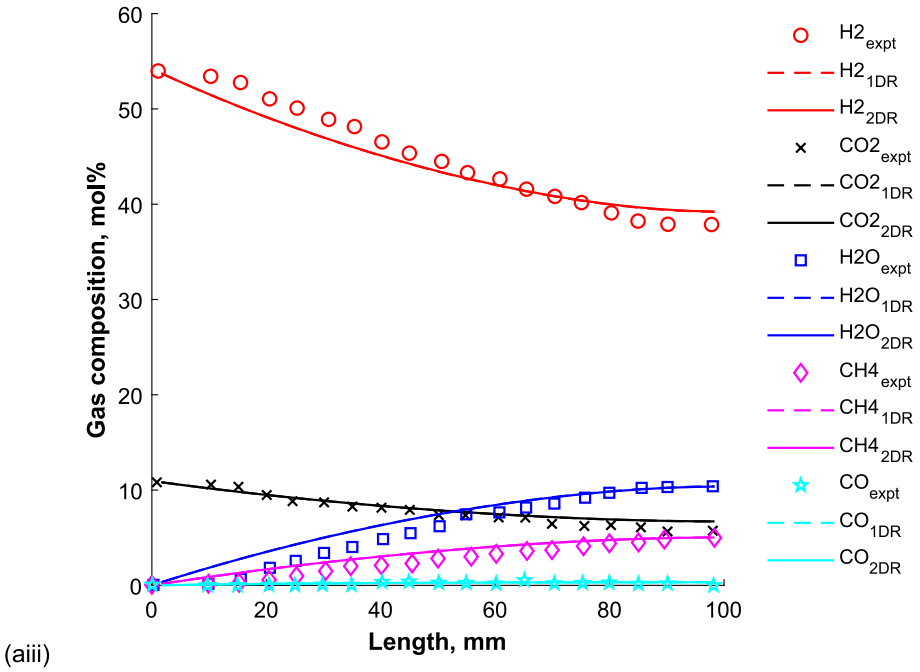

Fig. 4. (*continued*).

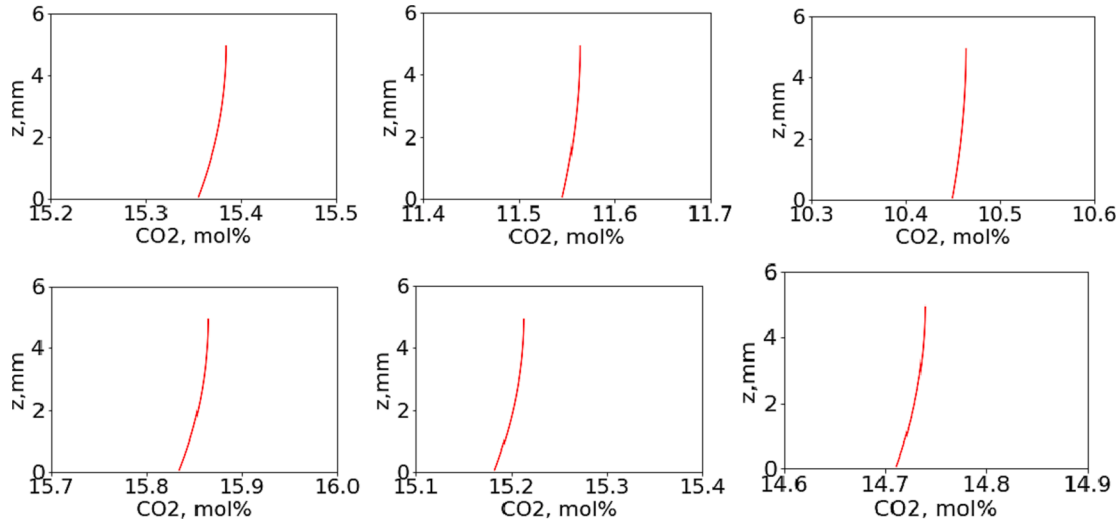

Fig. 5. Top row – $2D_{x\text{-}z}$ CFD model at 360 °C, 50 NmL min^{-1} and 1.2 bar at: (left) the channel entry where × = 5 mm, (middle) mid channel length where × = 55 mm and (right) channel exit where × = 98 mm. Bottom row' – $2D_{x\text{-}z}$ CFD model at 360 °C, 1500 NmL min^{-1} and 1.2 bar at: (left) the channel entry where × = 5 mm, (middle) mid channel length where × = 55 mm and (right) channel exit where × = 98 mm. An inlet feed of 64 mol% hydrogen, 16 mol% carbon dioxide, and 20 mol% argon was used. The CFD simulations in the bottom row are conducted at 30 times the flowrate of the CFD simulations in the top row.

(Hernandez Lalinde, 2020) compared 20 different LHHW rate expressions and showed, using a spatially resolved channel reactor and DRIFTS spectroscopy, that the kinetic model where the rate determining step includes the reaction of an oxygenated complex (HCOO*) with an active site (*) gives the closest agreement to experimental data. The kinetic parameters were determined under steady-state conditions in a spatially resolved channel reactor. Kopyscinski and co-workers used a 1D heterogeneous model (Hernandez Lalinde, 2020) to obtain kinetic parameters for carbon dioxide methanation in a channel reactor. They also used a 3D CFD model (Surendran, 2022) to assess the impact of the immersed sampling capillary on the quality of kinetic data obtained from the channel reactor. The CFD model included vital geometric features like inlet manifold and inlet/outlet distributor channels. At high flowrates, recirculation zones are created by submerged jets leaving the distributor channels.

During carbon dioxide methanation in laboratory-scale channel reactors, the flow develops and affects the concentration and temperature profiles generated during spatial characterisation. To improve the performance of carbon dioxide methanation systems, the influence of flow field on these profiles should be determined. Simulation of these interactions is an indispensable tool for further mechanistic understanding, reactor design and development. Although various kinetic and reactor models have been used to simulate carbon dioxide methanation over nickel-based catalysts (Weatherbee and Bartholomew, 1982; Inoue

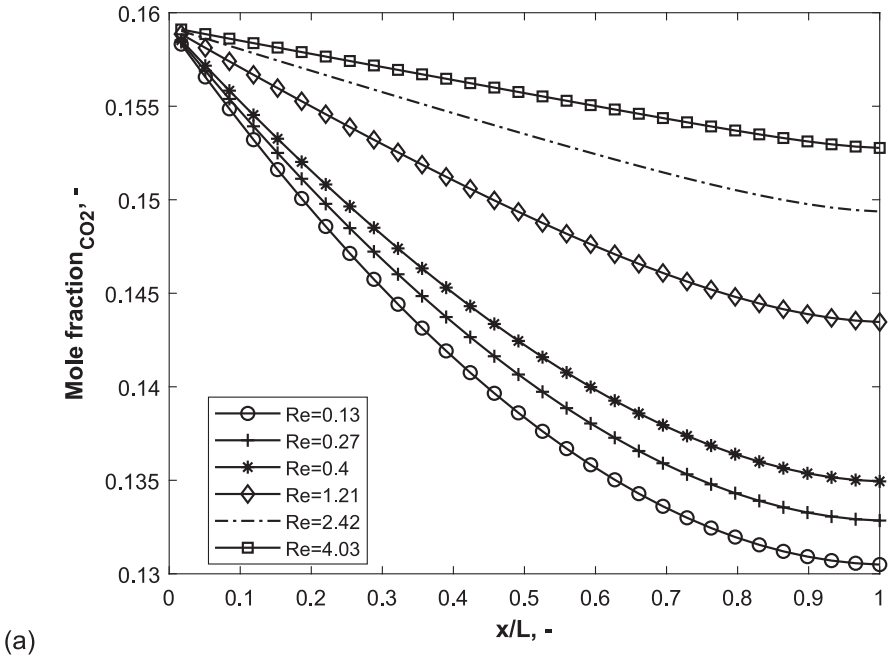

(a)

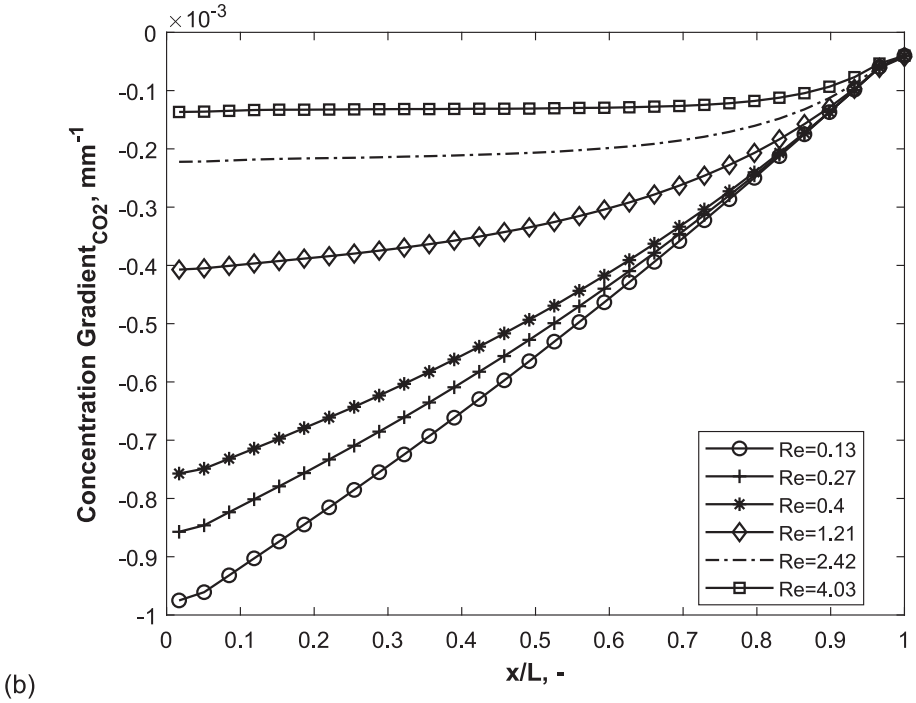

(b)

Fig. 6. (a) Composition (b) concentration gradient (c) rate gradient and (d) CO rate with channel length (e) CO yield-conversion (f) CH_4 yield-conversion with an inlet feed of 50—–1500 NmL min^{-1} in the spatially resolved channel reactor at 320 °C.

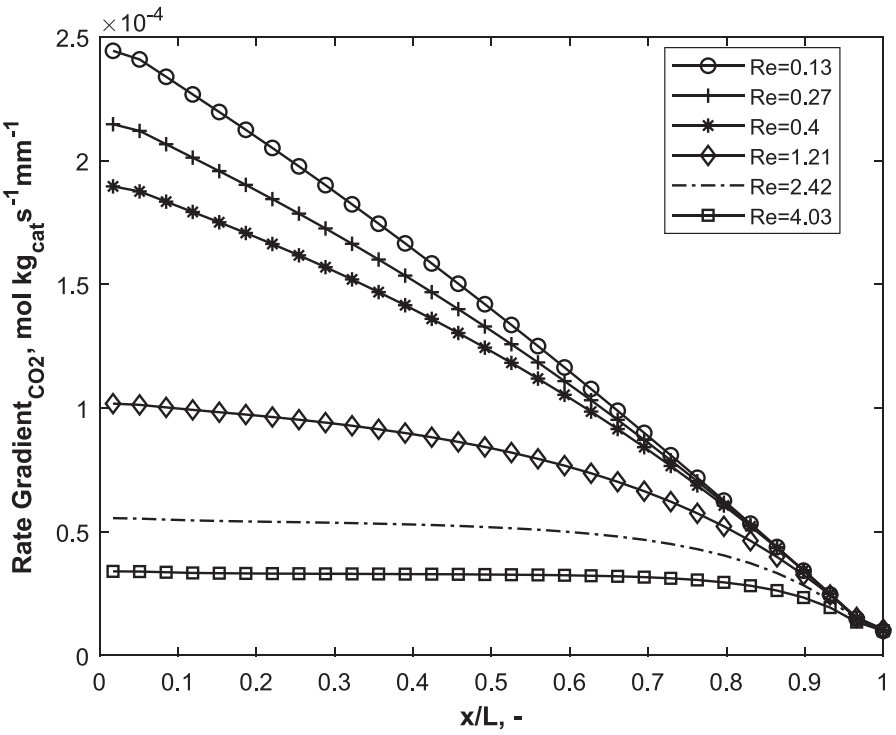

(c)

Fig. 6. (*continued*).

and Funakoshi, 1984; Hernandez Lalinde, 2020; Surendran, 2022; Chiang and Hopper, 1983; Van Herwijnen et al., 1973; Sughrue and Bartholomew, 1982), few models have considered the influence of flow on concentration profiles. Limited models and experimental studies have attempted to resolve the factors that govern steady-state performance of the channel reactor and connect the recently established mechanism to performance during steady-state runs of the channel reactor.

During kinetic studies in fixed bed reactors, differential rates are obtained. However, to obtain the reaction network during hydrocarbon conversion, high conversions ensue, and concentration and temperature gradients are observed. These gradients are either uniform or non-uniform at high conversions in a fixed bed reactor and although spatially resolved channel reactors provide an elucidation of the concentration and temperature gradients during kinetic measurements, there are limited studies on the characterisation of these gradients. Fewer studies have investigated the spatial resolution of the rates with respect to axial length and conversion and determination of the point at which kinetic control or external mass transfer dominates in relation to process parameters.

Consequently, in this paper, we aim to: (1) develop mechanism-performance relationships for the channel plate reactor, (2) characterise the uniformity of the gradients within the channel plate reactor, (3) investigate the influence of flow, pressure, temperature, H_2/CO_2 ratio, co-fed steam, and co-fed methane on these gradients and reactor performance, and (4) evaluate the utilisation of the reactor with relevance to kinetic modelling studies, catalyst design and reactor design. Using the LHHW mechanism and the kinetic model observed by Kopyscinski and co-workers for spatially resolved channel reactor experiments and DRIFTS spectroscopy (Hernandez Lalinde, 2020), we evaluate different reactor models for the channel reactor. We compare a 1D pseudo-homogeneous reactor model to a $2D_{x\text{-}z}$ pseudo-homogeneous reactor models and to archived reactor models (1D heterogeneous, 3D) for channel reactors. We evaluate the influence of flow on the axial and transverse concentration gradients. Carbon dioxide conversion, methane yields and selectivity, carbon monoxide yields, rates, concentration gradients and the interplay between intrinsic kinetics and mass transfer are characterised along the channel length, width, and height as we investigate the influence of flowrate, H_2/CO_2, co-feed of steam, and methane, at different reactor pressures and temperatures. We observe that the universal conversion limit of 5% for differential rates used in kinetic experiments in fixed bed reactors can be extended to 30% in channel plate reactors as differential rates, with negligible gradients and low external mass transfer influence, are observed at low temperatures during carbon dioxide methanation.

2. Methodology

2.1. Governing equations, model assumptions and boundary conditions

A 2D pseudo-homogeneous CFD model was constructed to obtain the velocity and concentration profiles from a channel reactor. The model was implemented in the Python CFD code called pyCALC-RANS (Davidson, 2021). The pyCALC-RANS is a finite volume code which solves the two-dimensional, steady incompressible momentum equations, the continuity equation and includes the k-ω turbulence model. The solution procedure is based on the pressure-correction method. The convection terms are discretized using a hybrid scheme of first-order upwind and second-order central differencing. The k-ω turbulence model was not utilised in our simulations. The 2D governing equations for reactive flow in the channel reactor are continuity, momentum, and mass conservation equations. The CFD code was adapted to include six specie balance equations. The experimental conditions (Hernandez Lalinde, 2020) used for the validation of the simulations show negligible temperature gradients (less than5 K). Consequently, the energy balance was not included in our investigation. Moreover, heat management

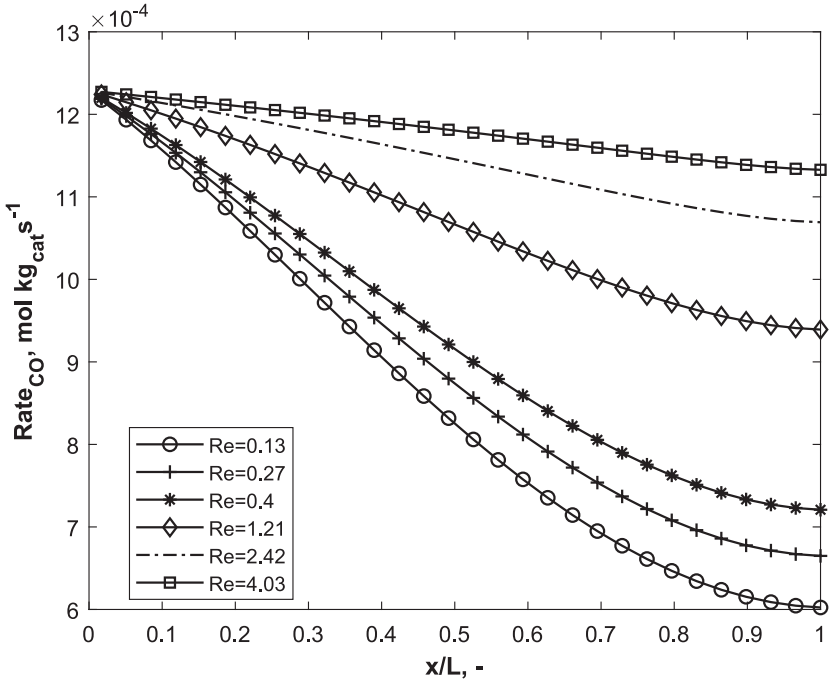

(d)

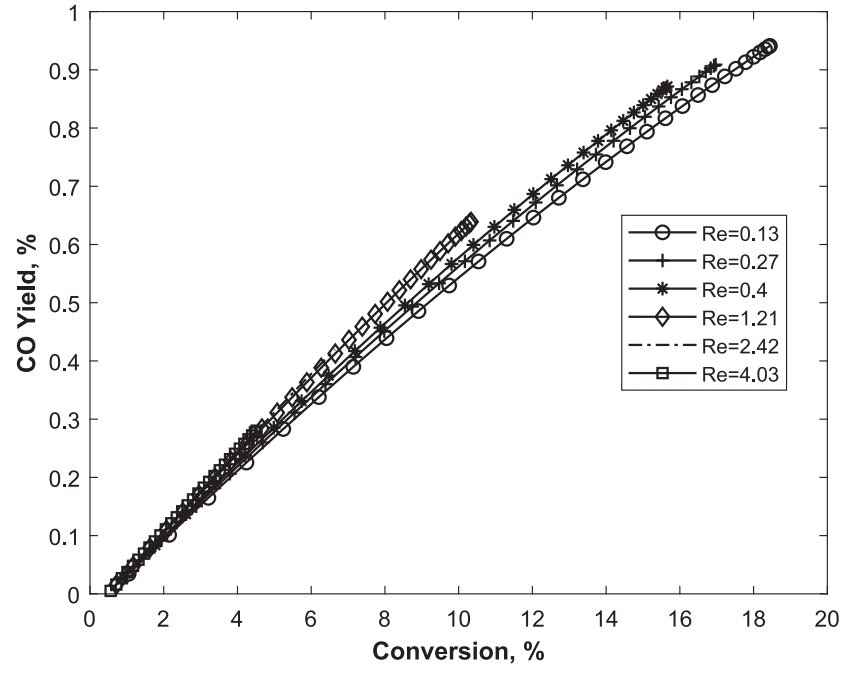

(e)

Fig. 6. (*continued*).

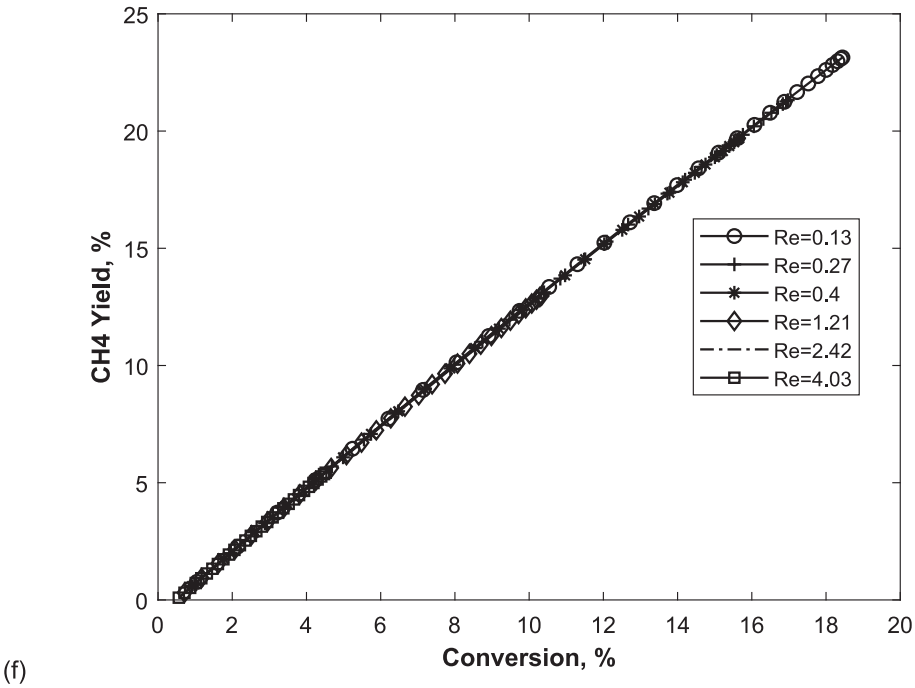

(f)

Fig. 6. (*continued*).

through thermal coupling has been investigated for other reactor concepts such as microchannel reactors and microreactors used for carbon dioxide methanation (Raghu and Kaisare, 2022; Engelbrecht et al., 2020). The following governing equations were used:

A. Continuity

$$\frac{\partial U}{\partial x}+\frac{\partial W}{\partial z}=0 \tag{1}$$

B. Momentum

$$\rho U\frac{\partial U}{\partial x}+\rho W\frac{\partial U}{\partial z}=-\frac{\partial P}{\partial x}+\mu\frac{\partial^2 U}{\partial x^2}+\mu\frac{\partial^2 U}{\partial z^2} \tag{2}$$

$$\rho U\frac{\partial W}{\partial x}+\rho W\frac{\partial W}{\partial z}=-\frac{\partial P}{\partial z}+\mu\frac{\partial^2 W}{\partial x^2}+\mu\frac{\partial^2 W}{\partial z^2} \tag{3}$$

C. Specie

$$\rho U\frac{\partial w_i}{\partial x}+\rho W\frac{\partial w_i}{\partial z}=\rho D_i\frac{\partial^2 w_i}{\partial x^2}+\rho D_i\frac{\partial^2 w_i}{\partial z^2}+R_{i,g} \tag{4}$$

where U and W are × and z components of velocity (m/s), w_i is the mass fraction of specie, I (-), P is pressure (Pa), ρ is density (kg m^{-3}), μ is dynamic viscosity (kg m^{-1} s^{-1}), D_i is diffusivity (m^2/s), $R_{i,g}$ is the rate of reaction (kg m^{-3} s^{-1}). The viscosity and diffusivity were calculated using Lennard-Jones parameters and collision integrals obtained from Bird, Stewart and Lightfoot (Bird et al., 2007).

The computational domain represents two-dimensional channel flow during carbon dioxide methanation. The computational domain (length by width) was 0.054 m by 0.04 m. For model validation, the computational domain was extended to 0.1 m by 0.04 m (Fig. 1). The channel depth was kept at 0.005 m. The set of equations (1)–(4) represent a $2D_{x\text{-}z}$ model. A 1D model will also be used.

2.2. $2D_{x\text{-}z}$ boundary conditions

A constant maximum velocity (x direction) was used at the left (western, x = 0) boundary with Neumann boundary conditions at the top (northern, z = D), bottom (southern, z = 0), and right (eastern, x = L) boundaries. Dirichlet boundary conditions were imposed on the left boundary for species with finite concentrations. Neumann boundary conditions were set at the top, bottom and right boundaries for species except argon, where Dirichlet conditions were set on the top and bottom boundaries. The channel length was divided into 30 cells and the channel depth was set to 32 cells.

where w_i is the mass fraction of species except argon, $w_{Ar,feed}$ is the mass fraction of argon in the feed, $w_{i,feed}$ is the mass fraction of the inlet feed. D is the channel depth, and L is the channel length, x is coordinate axis along the channel length and z is the coordinate axis along the channel depth. U_∞ is the maximum velocity, and W is the velocity component in the z direction. The origin of the coordinate axes was set to the left of the channel (Fig. 1). The number of global iterations was set to a maximum of 15,000 with a global convergence limit of 10^{-30}. The convergence limit for velocity, and for each specie was 10^{-6}.

The laboratory reaction rates, R_i (mol/s, kg_{cat}^{-1}) were re-defined as surface rates $R_{i,g}$ (kg m^{-3} s^{-1}) as they were determined close to the catalyst surface at z = 0. The surface rates, $R_{i,g}$, were multiplied by the area of the control volume. For the $2D_{x\text{-}z}$ model, the sampling position was placed 2 mm above the catalyst surface in accordance with experimental data (Lalinde et al., 2019; Hernandez Lalinde, 2020).

$$S_{x-z}=R_{i,g}\bullet A_{CV}\bullet\frac{Vol_{total}}{A_{total}} \tag{5}$$

where S_{x-z} is the source term in a computational control volume, $R_{i,g}$ is the surface rate, A_{CV} is the area of a control volume at z = 0, Vol_{total} is the

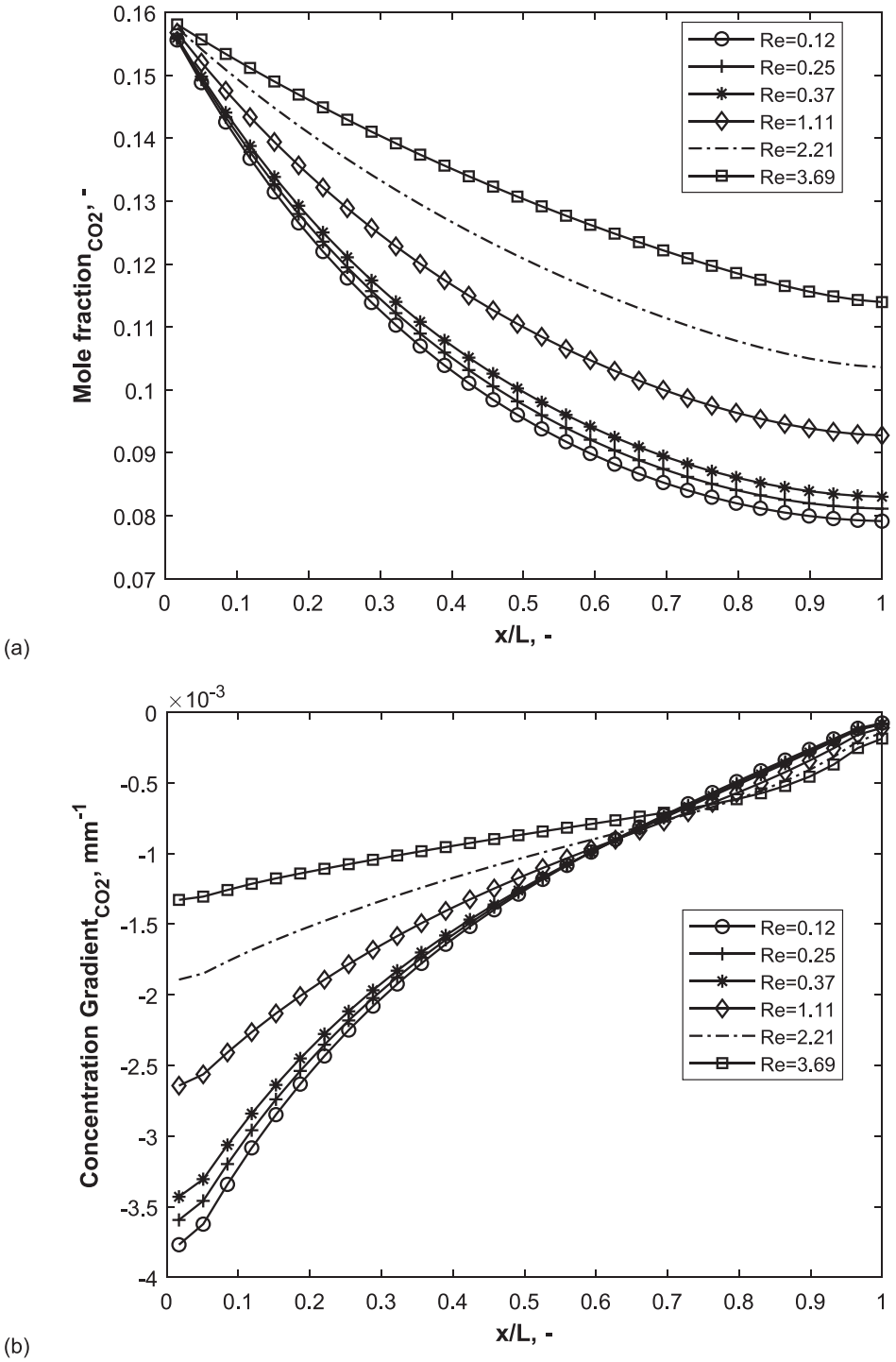

Fig. 7. (a) Composition (b) CO_2 concentration gradient (c) CO_2 rate gradient (d) CO rate (e) CO yield-conversion (f) CH_4 yield-conversion with an inlet feed of 50—–1500 NmL min^{-1}in the spatially resolved channel reactor at 400 °C.

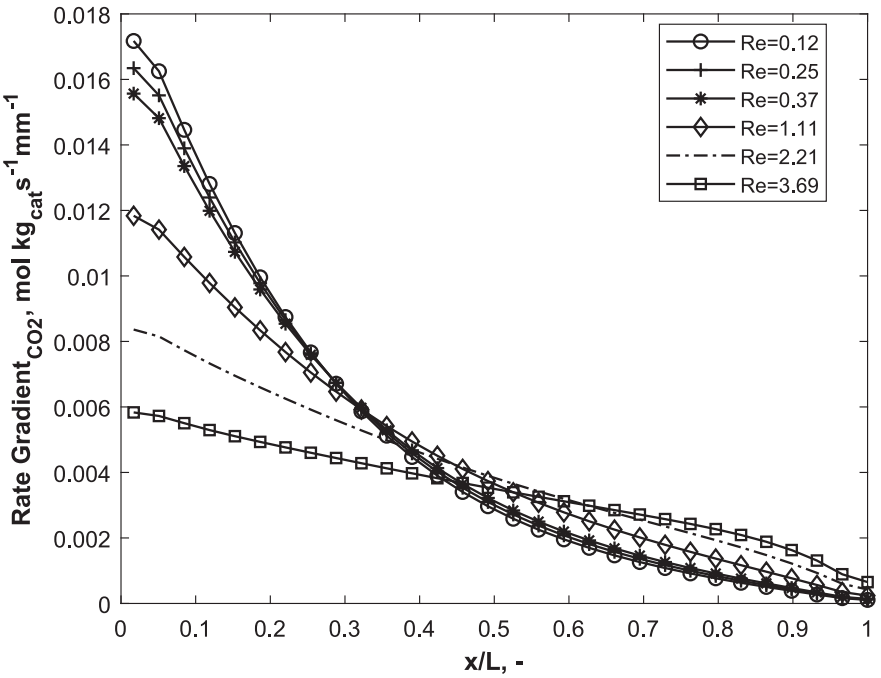

(c)

Fig. 7. (*continued*).

total volume of all cells in the computational domain, A_{total} is the sum of all areas of all cells at z = 0. For the $2D_{x\text{-}z}$ model, the sampling position was placed 2 mm above the catalyst surface in accordance with experimental data (Lalinde et al., 2019; Hernandez Lalinde, 2020).

2.3. 1D boundary conditions

For model comparison, the $2D_{x\text{-}z}$ CFD model was reduced to a $1D_x$ CFD model. In the 1D model, the channel length was divided into 30 cells and the channel depth was set to 1 cell. The surface rates were multiplied by the volume of a control volume (Vol_{CV}).

$$S_x = R_{i,g} \bullet Vol_{CV} \tag{6}$$

where S_x is the source along the x-domain and Vol_{CV} is the volume of a control volume.

2.4. Conversion, yield, and selectivity

The spatially resolved conversion of carbon dioxide, X_{CO2}, and spatially resolved selectivity (S_{CH4}) and yield (Y_{CH4}) to methane was defined, on a dry basis, in equations (7) – (9):

$$X_{CO2}(\%) = \frac{n_{CO2,in} - n_{CO2,\,inst}}{n_{CO2,in}} \times 100 \tag{7}$$

$$S_{CH4}(\%) = \frac{n_{CH4,inst}}{n_{CH4,inst} + n_{CO,inst}} \times 100 \tag{8}$$

$$Y_{CH4}(\%) = \frac{n_{CH4,inst}}{n_{CH4,inst} + n_{CO,inst} + n_{CO2,inst}} \times 100 \tag{9}$$

where $n_{CO2,in}$ is the inlet molar flow rate of carbon dioxide, $n_{i,inst}$ is the instantaneous flowrate of specie, i, defined at each cell of the computational grid.

2.5. Kinetics and rate equations

The LHHW kinetics governing the carbon dioxide methanation and the reverse water gas shift reaction are given by (Hernandez Lalinde, 2020):

$$r_1 = r_{CO2,meth} = \frac{k_{CO2,\,meth} \bullet K_{HCOO} \bullet p_{CO2} \bullet K_{H2}^{0.5} p_{H2}^{0.5} \bullet \left(1 - \left(\frac{p_{H2O}^2 \bullet p_{CH4}}{p_{H2}^4 \bullet p_{CO2} \bullet K_{eqM}}\right)\right)}{\left(1 + K_{HCOO} \bullet p_{CO2} \bullet K_{H2}^{0.5} \bullet p_{H2}^{0.5} + \sqrt{K_{H2} p_{H2}} + K_{OH} \frac{p_{H2O}}{\sqrt{p_{H2}}}\right)^2} \tag{10}$$

$$r_2 = r_{RWGS} = \frac{k_{RWGS} \bullet p_{CO2} \bullet K_{H2}^{0.5} \bullet p_{H2}^{0.5} \bullet \left(1 - \left(K_\beta \frac{p_{CO} \bullet p_{H2O}}{p_{H2} \bullet p_{CO2} \bullet K_{eqRWGS}}\right)\right)}{\left(1 + K_{HCOO} \bullet p_{CO2} \bullet K_{H2}^{0.5} \bullet p_{H2}^{0.5} + \sqrt{K_{H2} p_{H2}} + K_{OH} \frac{p_{H2O}}{\sqrt{p_{H2}}}\right)^2} \tag{11}$$

The laboratory reaction rates (R_i, mol/s kg_{cat}^{-1}) were given by the reaction rates for the species which were calculated using the following relations (r_1 for the reaction rate of carbon dioxide methanation, r_2 for the reaction rate of the reverse water gas shift reaction). The kinetic parameters are defined in Table 1.

$$R_{H2} = -4r_1 - r_2$$

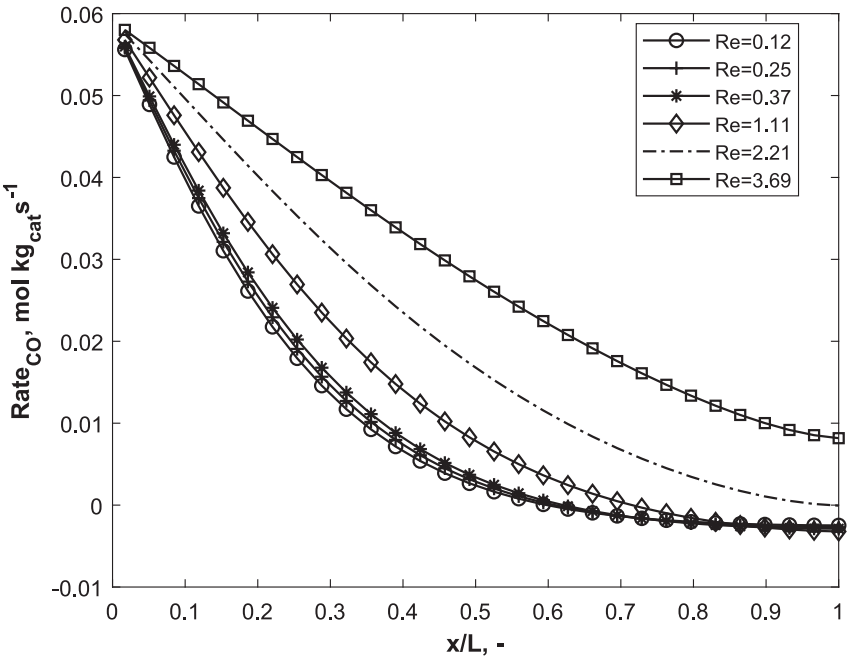

(d)

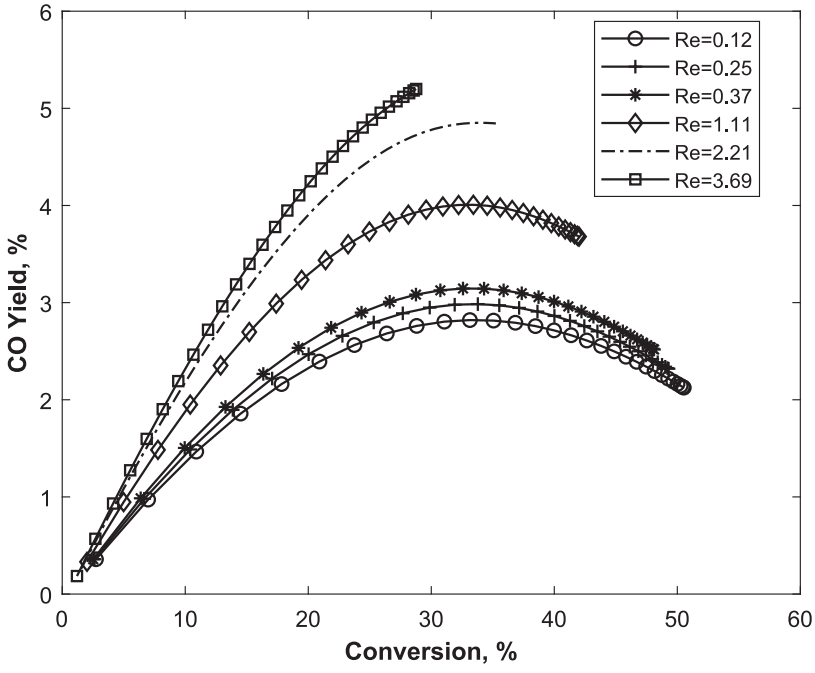

(e)

Fig. 7. (*continued*).

$R_{CO} = r_2$

$R_{CO2} = -r_1 - r_2$

$R_{CH4} = r_1$

$R_{H2O} = 2r_1 + r_2$

$R_{Ar} = 0$

Using similar kinetic parameters (Table 3) in the source terms, the reactor models (1D, 2D$_{x\text{-}z}$) were compared to each other. The reactor model with the best agreement to experimental data was used to investigate the connection between the mechanism and the performance of the channel reactor across different pressures, temperatures, compositions, and velocities.

The pre-exponential factors are based on the reference temperature (T_{ref} = 613.15 K = 340 °C). The rate equation for the reverse water gas shift also includes the water gas shift reaction, because of the small equilibrium constant (K_{eqRWGS} = 0.03 at 320 °C and 0.1 at 420 °C). The equilibrium constant for methanation is given as $K_{eqM} = 1 \times 10^5$ bar^{-2} at 320 °C and $K_{eqM} = 5 \times 10^2$ bar^{-2} at 420 °C.

The rates of methanation (r_1) and reverse water gas shift reaction (r_2) can each be expressed generally as:

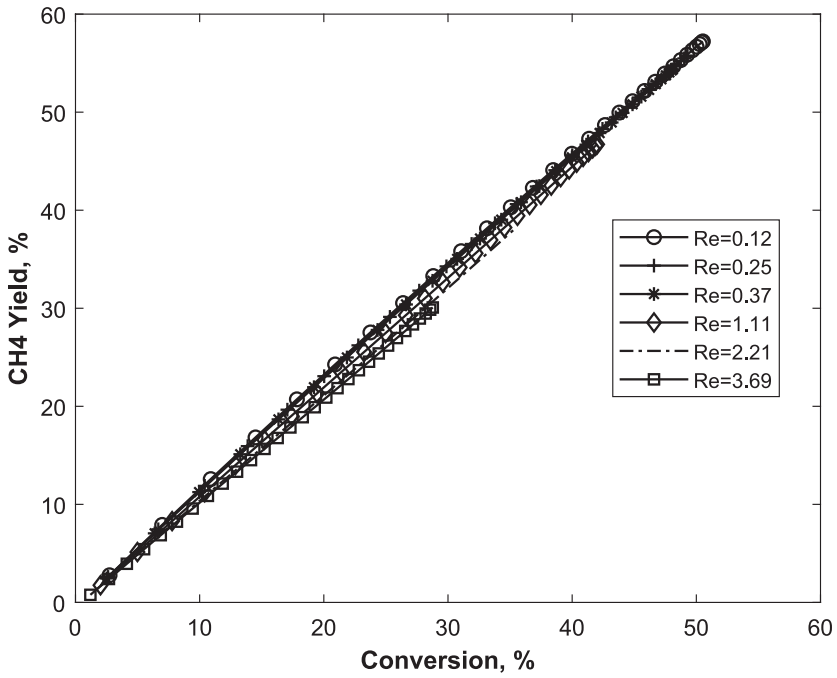

(f)

Fig. 7. (*continued*).

$$r = \frac{(rate\ constant) \times (driving\ force) \times (equilibrium\ term)}{adsorption\ term} \tag{12}$$

Rate decomposition of carbon dioxide methanation, and reverse water gas shift reaction can be found in Table 4.

2.6. External mass transfer control

Using the $2D_{x\text{-}z}$ pseudo-homogeneous model, the influence of external mass transfer on intrinsic kinetics will be evaluated in each cell. The influence of external mass transfer is evaluated along the channel length using the Carberry number. It gives the ratio of intrinsic kinetics to convective effects. The Carberry number (Ca) for catalytic channel plate reactors can be derived as (Kopyscinski et al., 2010):

$$Ca = \frac{l_{ch} \bullet \omega_{cat} \bullet R_i}{b \bullet Sh \bullet D_{i,mix} C_{b,i}} \tag{13}$$

where l_{ch} is the characteristic length (m), ω_{cat} is the catalyst length density ($kg_{cat}\ m^{-1}$), b is the width of the catalyst plate (m), Sh is the Sherwood number (-), $D_{i,mix}$ (m^2/s) is the diffusion coefficient of specie, i in the gas mixture, $C_{b,i}$ is the bulk gas concentration of species (mol/m^{-3}(−|-)). A Sherwood number of 3.7 is used, as determined for catalytic combustion in a monolith reactor at low Reynolds numbers (Raja et al., 2000).

$$D_{i,mix} = \frac{1 - x_i}{\sum_j x_j / D_{i,j}} \tag{14}$$

$$D_{i,j} = 0.0018583 \sqrt{T^3 \left(\frac{1}{M_i} + \frac{1}{M_j}\right)} \frac{1}{p \sigma_{ij}^2 \Omega_{D,ij}} \tag{15}$$

where M_i and M_j refer to the molecular weight of species i, and j, $\Omega_{D,ij}$ is the collision integral of species i and j, $\sigma_{i,j}$ is the Lennard-Jones parameter of specie I, and j, x_i and x_j are the mole fractions of specie, i and j, respectively.

3. Results and discussion

3.1. Model validation

The reactor models were validated against experimental data obtained by Kopyscinski and co-workers (Hernandez Lalinde, 2020) on carbon dioxide methanation and the competing reverse water gas shift reaction. The kinetics of carbon dioxide methanation and the competing reverse water gas shift reaction was determined using a combined methodology that includes spatially resolved channel reactor experiments and DRIFTS spectroscopy (Hernandez Lalinde, 2020). According to Kopyscinski and co-workers, the model that assumes that the hydrogen-assisted C-O bond cleavage from adsorbed HCOO* gives a better agreement to spatially resolved channel reactor data and DRIFTS spectroscopy (Hernandez Lalinde, 2020). To validate our work, we compared our 1D pseudo-homogeneous (1DR) simulations and $2D_{x\text{-}z}$ pseudo-homogeneous (2DR) simulations to the experimental and computational work of Kopyscinski and co-workers (Lalinde et al., 2019; Hernandez Lalinde, 2020; Surendran, 2022).

The 1D and $2D_{x\text{-}z}$ CFD model give good agreement with experimental data at 320 °C (Fig. 2a) and at 400 °C, there is good agreement upstream and a fair agreement downstream for carbon dioxide methanation (Fig. 2b). Specifically, at 400 °C, we observe deviations between the simulations and experimental profiles of hydrogen and methane downstream of the channel reactor. The simulations of the concentration profiles of carbon monoxide, carbon dioxide, and water agree well with experimental data. Kopyscinski and co-workers (Hernandez Lalinde, 2020) used a 1D two-phase reactor model (1D) to simulate the experimental data obtained from a channel plate reactor. The $2D_{x\text{-}z}$ pseudo-homogenous model accounts for concentration changes along the channel length and channel depth. In Fig. 3, we compare spatially resolved channel experimental data to the 1D two-phase reactor model (1D) of Kopyscinski and co-workers (Hernandez Lalinde, 2020) and the 1D pseudo-homogeneous CFD (1DR) and $2D_{x\text{-}z}$ pseudo-homogeneous CFD (2DR) model. At both temperatures, the 1D CFD model performs as well as the 1D two-phase model of Kopyscinski and co-workers. Nonetheless, there is a better agreement between experimental data and the 1DR model downstream of the channel reactor (Fig. 3aii and

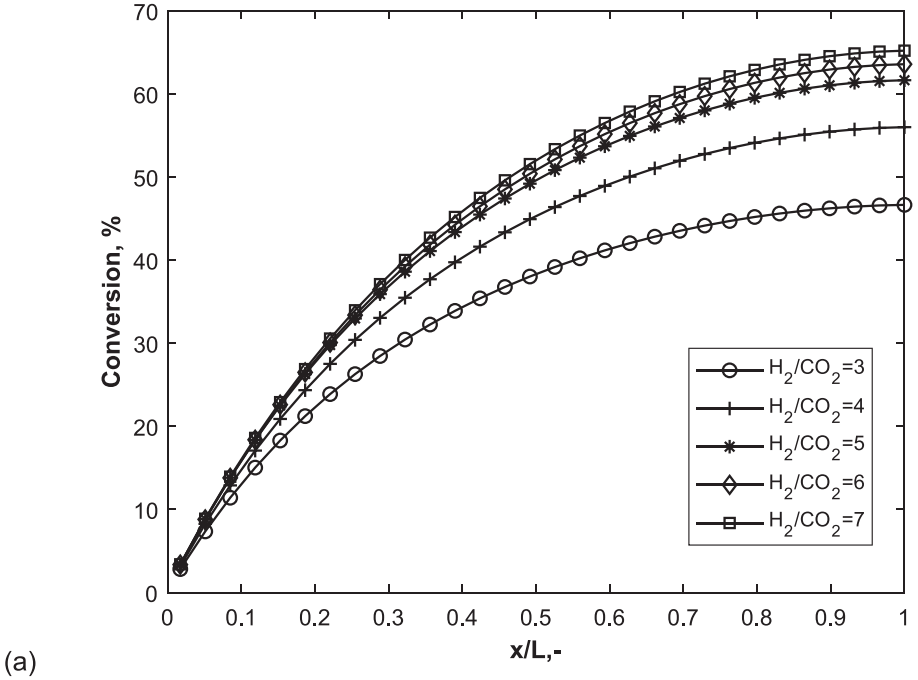

(a)

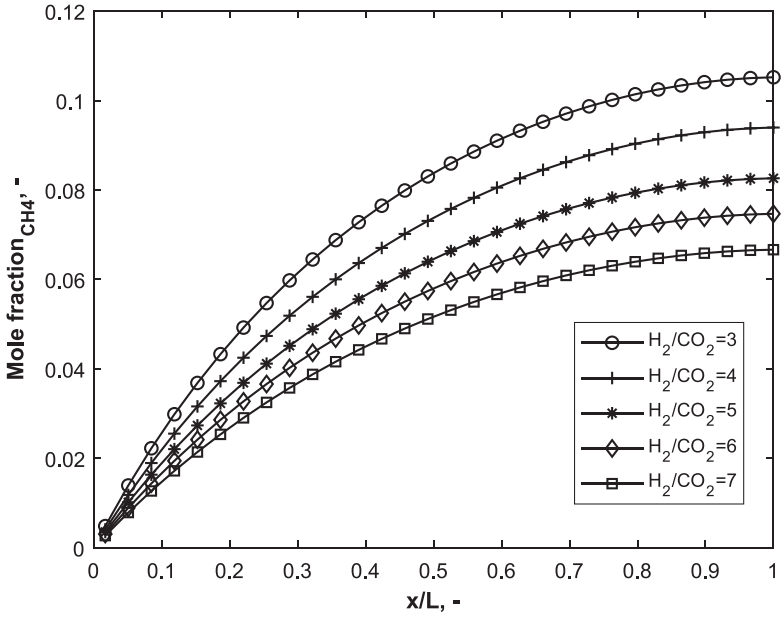

(b)

Fig. 8. (a) Conversion (b) CH_4 composition (c) concentration gradient (d) CO composition (e) CO yield (f) CH_4 yield-conversion for H_2/CO_2 ratio of 3–7 in the spatially resolved channel reactor at 400 °C, 1.2 bar and 100 NmL $min^{-1.}$

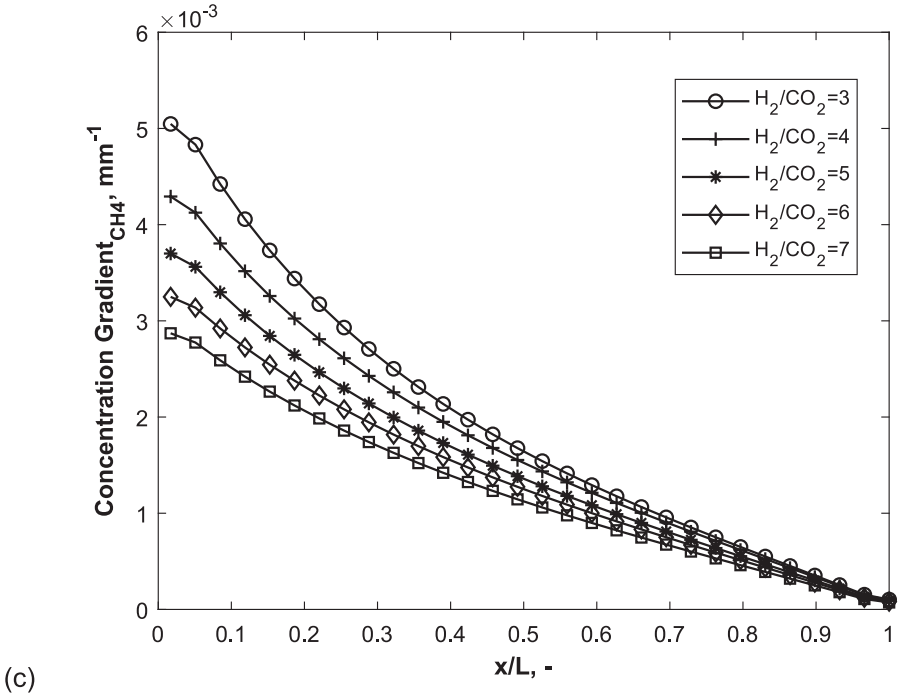

(c)

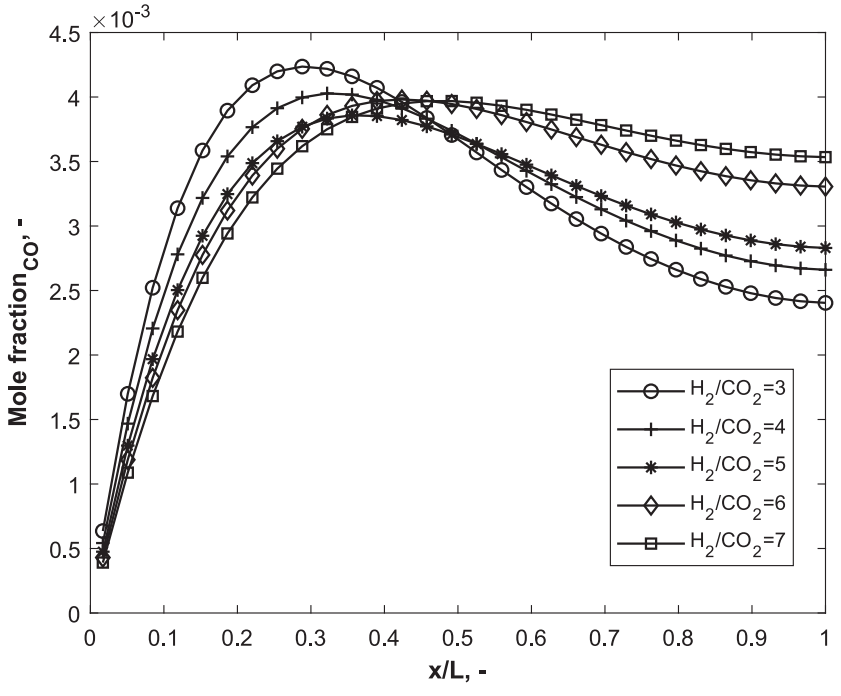

(d)

Fig. 8. (*continued*).

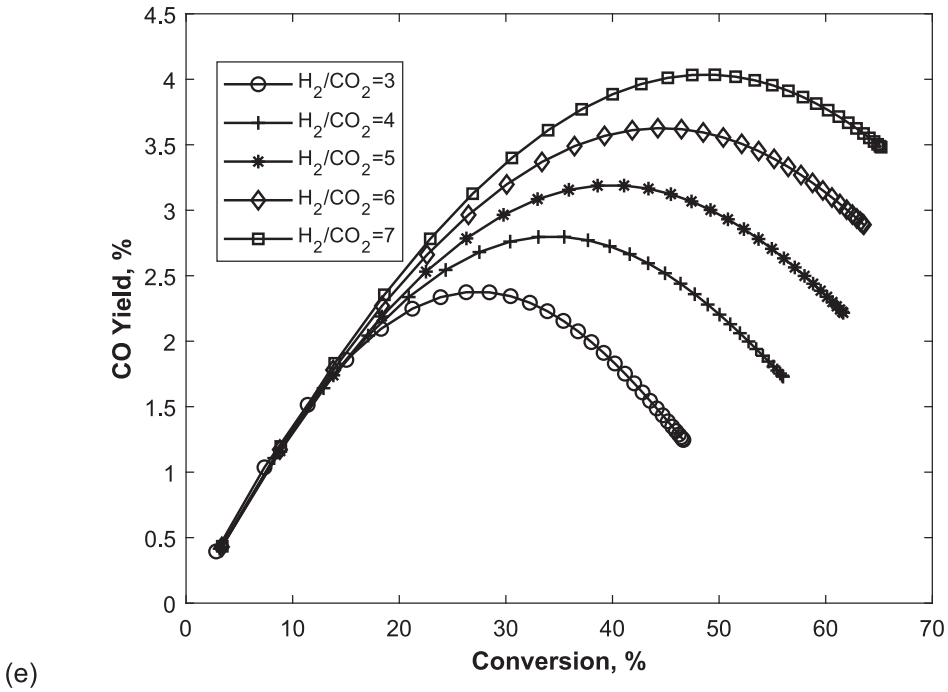

(e)

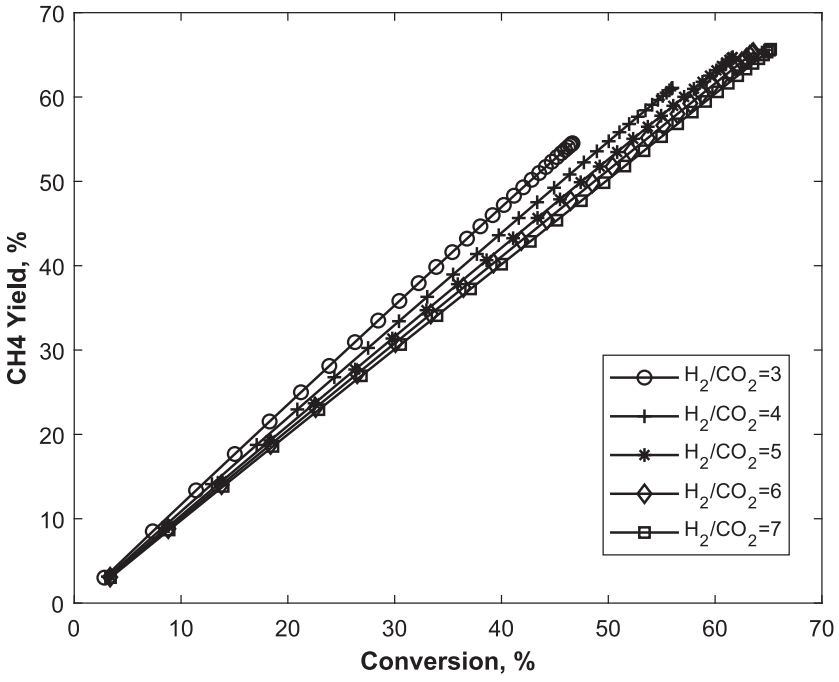

(f)

Fig. 8. (*continued*).

3bii). The results from the $2D_{x\text{-}z}$ CFD (2DR) model are similar to the 1D CFD (1DR) model (Fig. 3aiii and 3biii).

In Fig. 4, we compare our 1D CFD reactor (1DR) model and $2D_{x\text{-}z}$ CFD reactor (2DR) model to the 1D two-phase reactor (1D) model (Hernandez Lalinde, 2020), and 3D reactive CFD reactor (3D) model (Surendran, 2022). The 3D reactive CFD model compares favourably with the $2D_{x\text{-}z}$ CFD model. Although the 3D CFD model shows a higher accuracy in predicting the concentration profiles of water, and methane, the $2D_{x\text{-}z}$ CFD model shows higher accuracy for carbon dioxide and hydrogen profiles. Furthermore, the $2D_{x\text{-}z}$ CFD model performs equally as good as the 1D CFD model.

3.2. Model specification

The variation in concentration of species with channel depth has been observed previously in channel plate reactor studies (Hernandez Lalinde, 2020). We chose the $2D_{x\text{-}z}$ model as it allows for the simulation of changing concentration profiles with depth across the channel plate reactor. Fig. 5 shows a variation in specie concentration along the channel depth although dirichlet boundary conditions were set for the mass fraction of species at the channel entry. In the $2D_{x\text{-}z}$ model, this variation in concentration of the species along the channel depth (z direction) is attenuated towards the channel exit. The change in specie concentration with channel depth is strengthened with increasing

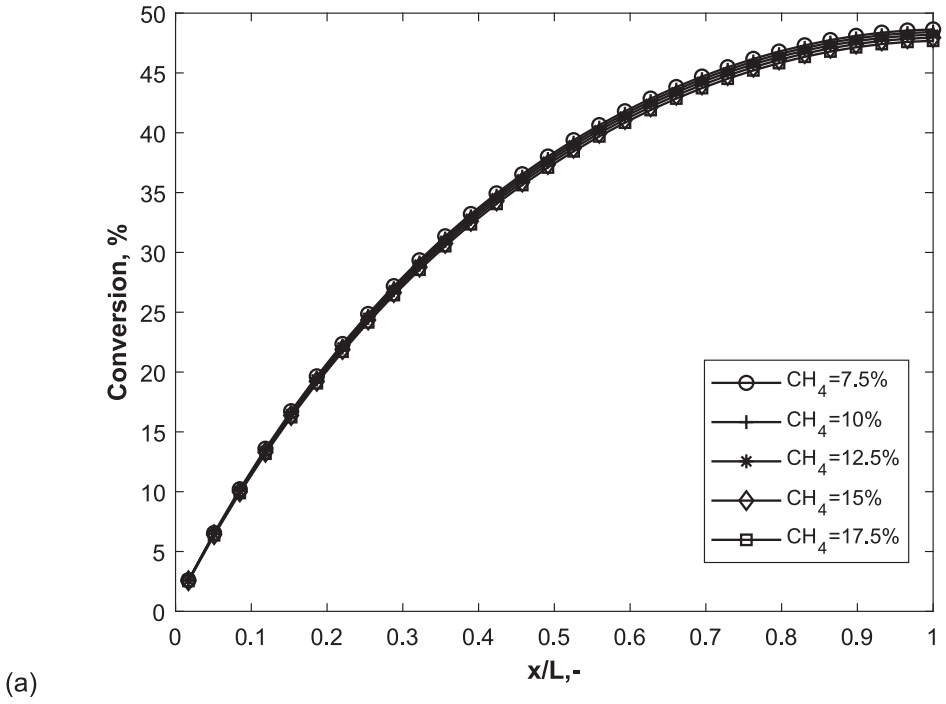

(a)

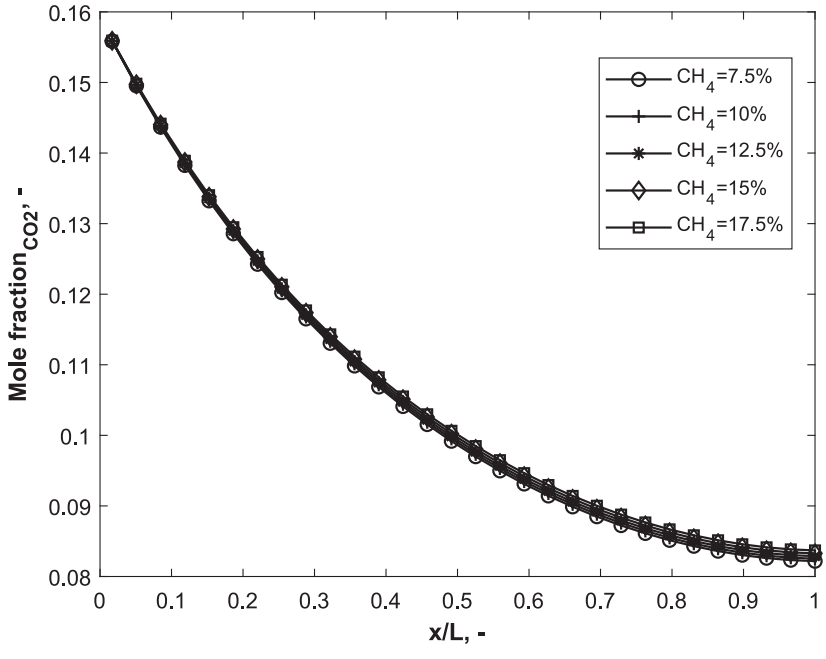

(b)

Fig. 9. (a) Conversion (b) CO_2 composition (c) concentration gradient (d) CO composition (d) CO yield-conversion (e) Carberry numbers obtained with co-feeding methane at 7.5% − 17.5% in the spatially resolved channel reactor at 400 °C and 1.2 bar and 100 NmL min^{-1} at a constant H_2/CO_2 ratio of 4.

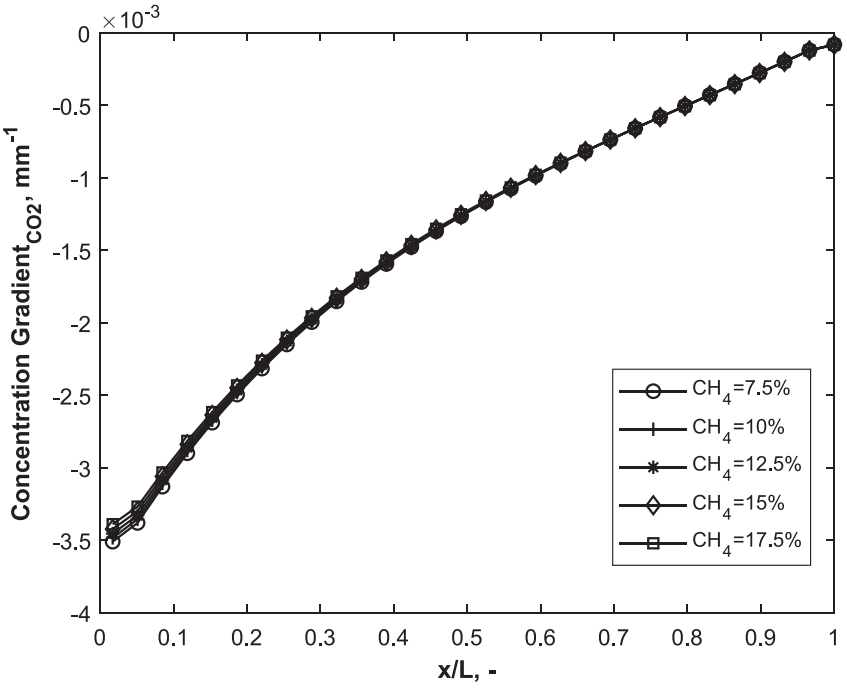

(c)

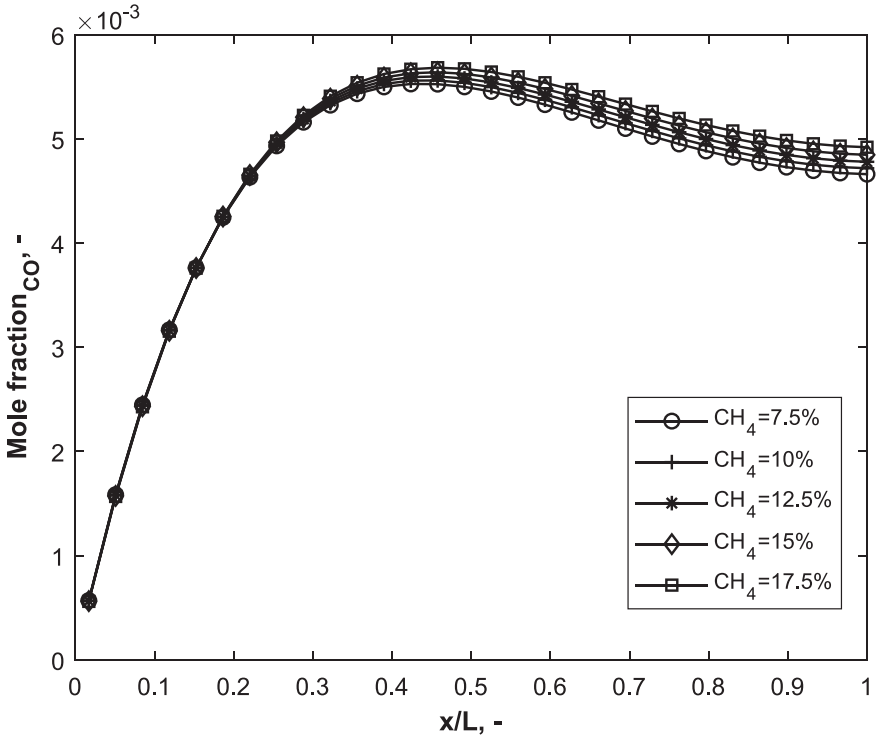

(d)

Fig. 9. (*continued*).

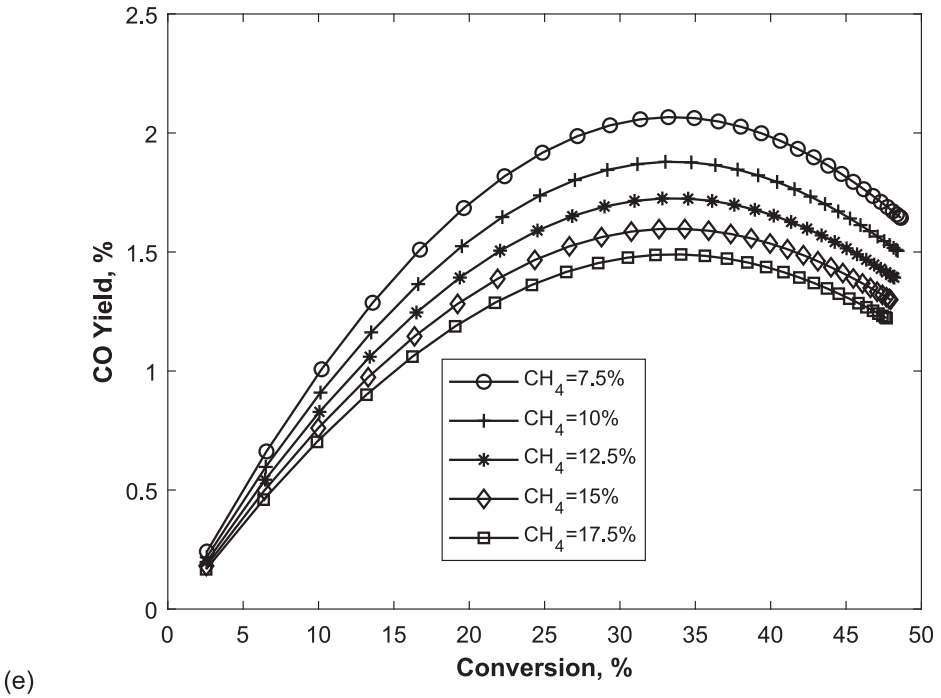

(e)

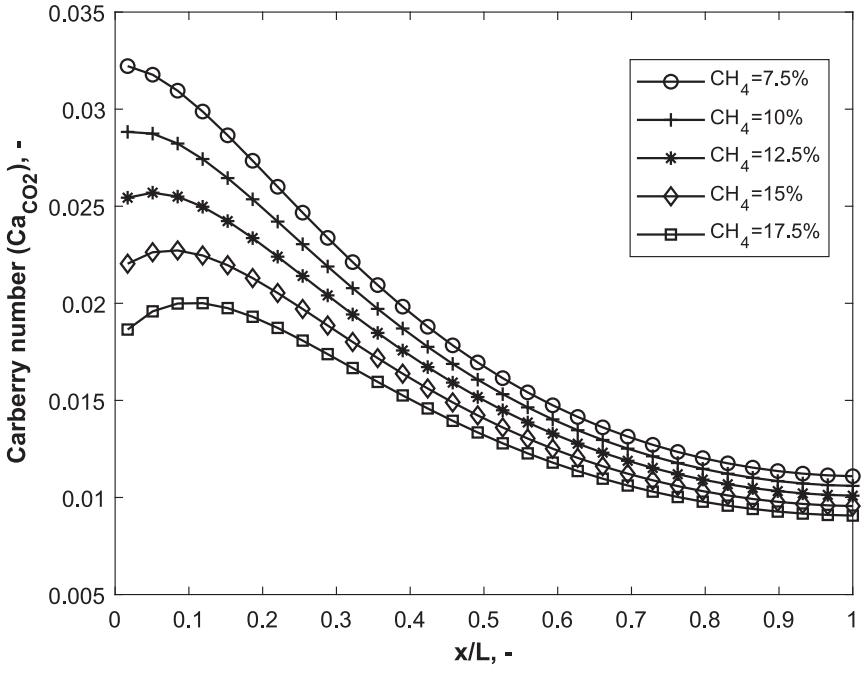

(f)

Fig. 9. (*continued*).

flowrate through the channel.

Using the $2D_{x\text{-}z}$ model, the effect of grid resolution was conducted at 1500 NmL min^{-1}, 1.2 bar and 320 °C with 64 mol% hydrogen, 16 mol% carbon dioxide, and 20 mol% argon using a 30 × 32 grid and a 15 × 16 grid (see figure S1 of the supplementary information). We observe that the grid has no influence on the $2D_{x\text{-}z}$ CFD simulations. Consequently, we have a grid-independent study. Furthermore, we evaluate the influence of flowrate, H_2/CO_2 ratio, methane co-feed, steam co-feed, pressure, and temperature using the $2D_{x\text{-}z}$ model.

3.3. Influence of flowrate

At 320 °C, flow in the channel reactor lies in the laminar range. The feed (and the Reynolds number) for the spatially resolved channel reactor is given at 50 NmL min^{-1} (0.13), 100 NmL min^{-1} (0.27), 150 NmL min^{-1} (0.4), 450 NmL min^{-1} (1.21), 900 NmL min^{-1} (2.42) and 1500 NmL min^{-1} (4.03). We observe that the concentration and rate profiles across reactants (carbon dioxide, hydrogen) are similar, and the concentration and rate profiles across products (methane, water) are similar except for carbon monoxide (Fig. 6a-d and section S2 in supplementary information) whose overall profile shape is temperature dependent. The uniformity of the rate and concentration gradients were

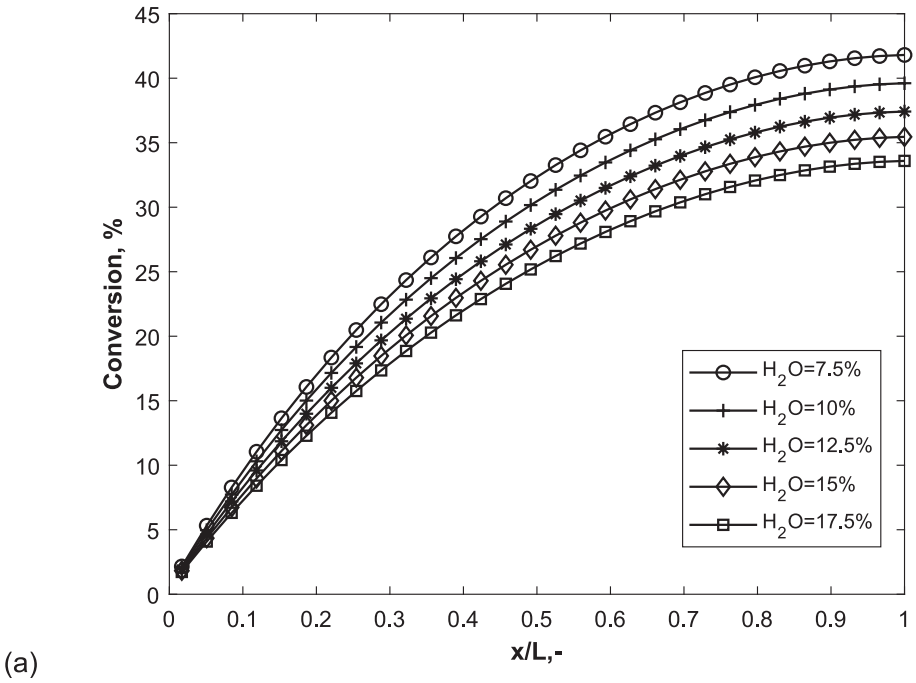

Fig. 10. (a) Conversion (b) CO_2 composition (c) concentration gradient (d) CO yield-conversion (e) CH_4 yield-conversion (f) Carberry number determined with co-feeding steam at 7.5% − 17.5% in the spatially resolved channel reactor at 400 °C and 1.2 bar and 100 NmL min^{-1} at a constant H_2/CO_2 ratio of 4.

evaluated using the concentration profiles defined along the axial length (x-dimension) of the channel reactor.

The rate of consumption of reactants i.e., carbon dioxide, and hydrogen, increases with an increase in flow rate and reduces with channel length. The gradient of the rate of consumption of carbon dioxide, and hydrogen decreases with flow rate and along the channel length of the reactor (Section S2 in supplementary information and Fig. 6b and Fig. 6c). The rate of methane production is given by the rate of methanation (r_1) and the rate of carbon monoxide transformation is given by the rate of the reverse water gas shift reaction (r_2). Likewise, the rate of generation of products i.e., methane, water, and carbon monoxide increase with an increase in flowrate and reduces with channel length. The gradient of the rate of production of methane, water, and carbon monoxide decreases with flow rate and along the channel length of the reactor. Consumption and production rates (Fig. 6d) for Re less than 1 are clustered together and separated from flow where Re > 1.

The gas composition of the reactants (carbon dioxide, hydrogen) decreases across the channel length but increases with flowrate leading to a decrease in conversion with an increase in flow rate (Fig. 6a-d). The gradients in reactant compositions across the channel length reduce as flow rate increases. On the other hand, the gas compositions of the products (carbon monoxide, water, methane) increase across the channel length but decreases with an increase in flow rate while the gradients in product compositions across the channel length behave similar to the gradients in reactant compositions, that is, they reduce as flowrate increases.

Conversion and selectivity reduce with an increase in flowrate. At lower than 5% conversion obtained at 1500 NmL min^{-1}, Re = 4.03 (see Fig. S2c in supplementary information), differential rates are obtained as observed for fixed bed reactors. Consequently, there are negligible gradients in the rates of consumption and production of species under these conditions. The yield of carbon monoxide (Fig. 6e), and methane (Fig. 6f) increase linearly with conversion.

With an increase in temperature, at 400 °C, flow in the channel reactor still lies in the laminar range. In Fig. 7, the feed (and the Reynolds number) into the spatially resolved channel reactor is given at 50 NmL min^{-1} (0.12), 100 NmL min^{-1} (0.25), 150 NmL min^{-1} (0.37), 450 NmL min^{-1} (1.11), 900 NmL min^{-1} (2.21) and 1500 NmL min^{-1} (3.69).

The spatial gas composition of the reactants (carbon dioxide, hydrogen) decrease across the channel length but increase with flowrate leading consequently to a decrease in conversion with flowrate (Fig. 7a). The spatial gas composition of methane increase with channel length and reduce with flowrate. The gradients in carbon dioxide and methane compositions reduce with flowrate up until midway (x/L = 0.65) through the channel reactor, then increase with flowrate downstream of the channel reactor (Fig. 7b). Conversion and selectivity both increase with channel length but reduce with an increase in volumetric flowrate.

The rate of consumption of carbon dioxide, and hydrogen increases with an increase in flow rate and reduces with channel length. The gradient of the rate of consumption of reactants (e.g., carbon dioxide) and products (e.g., methane) decreases with flow rate up until about x/L = 0.35 (Fig. 7c). About midway through the reactor towards the channel exit, the gradient of the rate of reactant consumption and product formation increases with flow rate through the channel reactor. Consumption and production rates for Re less than 1 are clustered together and separated from Re > 1 (Fig. 7d). This clustering effect is more significant at higher temepratures (400 °C) compared to lower temperatures (320 °C).

There is a maximum in the carbon monoxide concentrations across the channel length at 400 °C. This maximum stays fairly constant for Re less than 1 and increases for Re > 1. The maximum in carbon monoxide composition results in the rates of carbon monoxide production cycling between formation (+ve) and consumption (-ve) with the transition point moving downstream as flowrate increases from 50 to 900 NmL min^{-1}. At high flowrates, 1500 NmL min^{-1}, the rate of carbon monoxide production is positive along the channel length (Fig. 7d).

On comparing the influence of flow on the performance of carbon dioxide methanation, at low temperatures, the carbon monoxide yield increases linearly with conversion and as temperature increases, the carbon monoxide yield reaches a maximum with conversion (Fig. 6e,

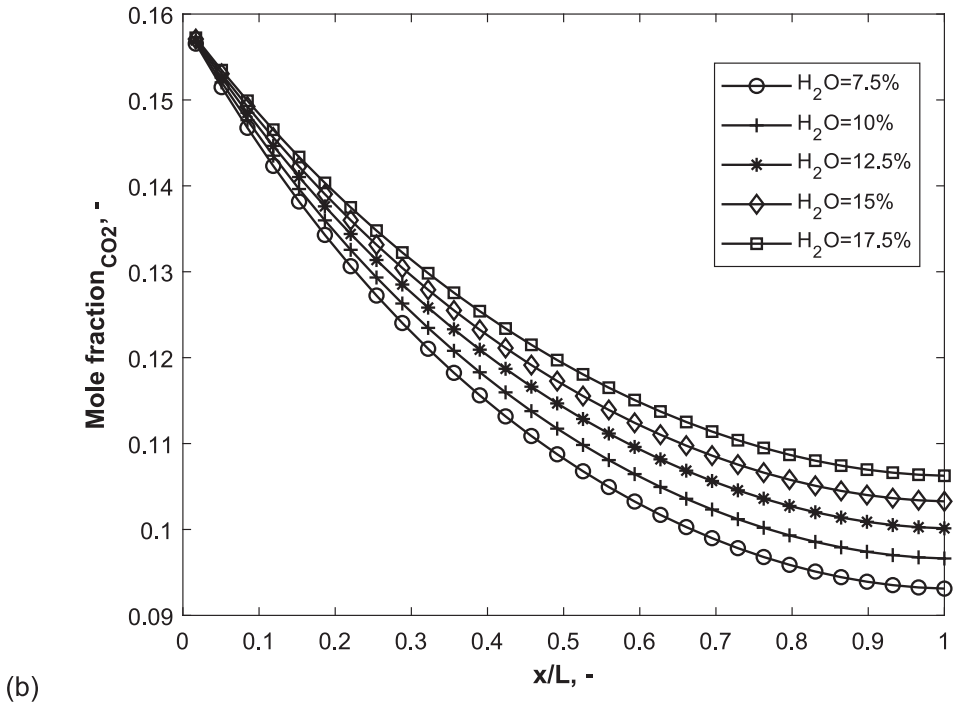

(b)

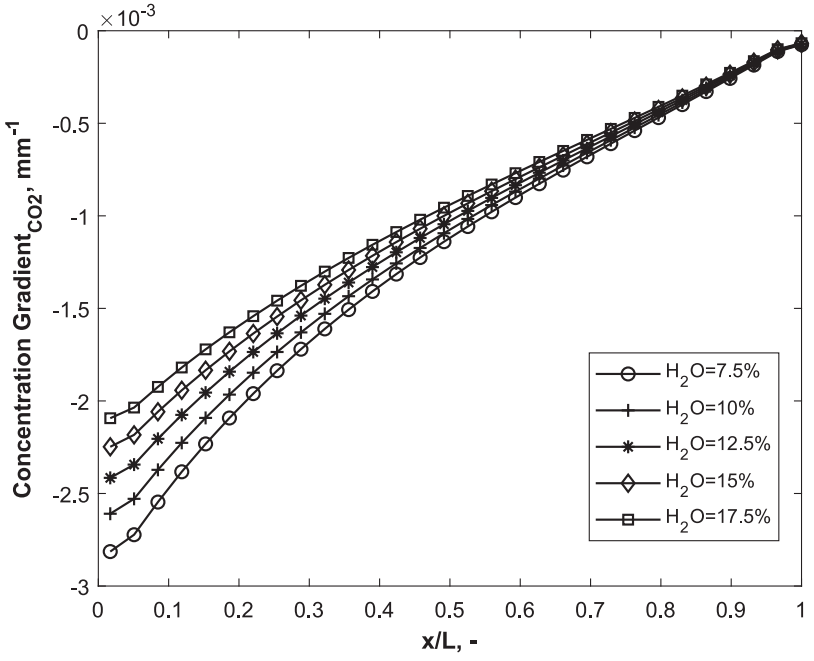

(c)

Fig. 10. (*continued*).

and 7e). Conversely, the methane yield increases linearly with conversion at all flowrates (Fig. 6f and 7f). A maximum methane yield of ~ 60% at *ca.* 50% conversion is obtained from variation in flowrates at 400 °C. Consequently, the influence of flow rate on concentration profiles is temperature-dependent.

3.4. Influence of H_2/CO_2 ratio

Conversion increases with an increase in H_2/CO_2 ratio in the channel reactor (Fig. 8a). Kolb and co-workers (Lefebvre et al., 2015) reported an increase in reactor performance with an increase in H_2/CO_2 ratio for a slurry bubble column reactor. Upstream of the channel reactor, between H_2/CO_2 of 5 – 7, there are no changes in conversion with channel length (Fig. 8a). The major changes in the conversion that take place with H_2/CO_2 ratio occur downstream of the channel reactor. The composition of methane and water follow the same trend, that is, the outlet concentrations reduce with an increase with H_2/CO_2 ratios with H_2/CO_2 of 7 showing the smallest concentration gradients (Fig. 8b and 8c). There is a maximum variation in concentration gradient, as the H_2/CO_2 ratio is increased, towards the channel entry at x/L = 0.08. With an increase in H_2/CO_2 ratio, the maximum in CO concentration reduces and moves further downstream of the channel reactor. This maximum is exhibited in carbon monoxide profiles with H_2/CO_2 ratio across the axial length of the channel reactor (Fig. 8d).

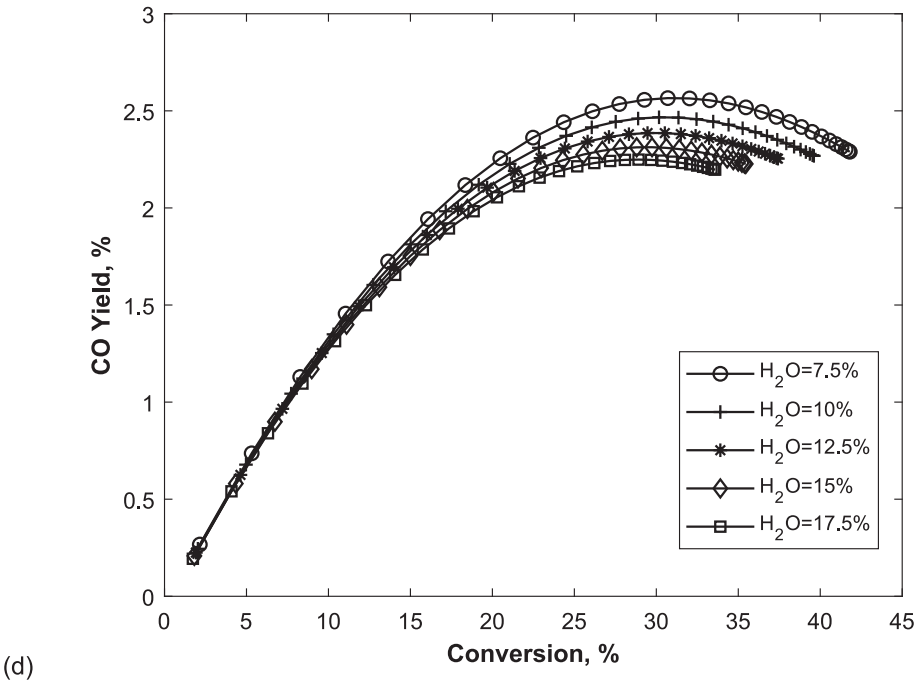

Fig. 10. (*continued*).

The yield of carbon monoxide exhibits a maximum with carbon dioxide conversion (Fig. 8e). This maximum increases and moves further downstream of the channel reactor as H_2/CO_2 ratio increases. This is due to the increasing significance of reverse water gas shift reaction along the channel length as H_2/CO_2 ratio increases. Across all H_2/CO_2 ratios, the flow remains in the laminar range. Methane yield increases linearly with conversion. At a fixed conversion, there is a higher methane yield at lower H_2/CO_2 ratios (Fig. 8f).

Convective effects increase with channel length and with H_2/CO_2 ratio. Intrinsic rates of carbon dioxide consumption decrease with increasing H_2/CO_2 ratios up to a locus at $x/L = 0.2$, whereupon it increases with increasing H_2/CO_2 ratio. Overall, the Carberry number increases with H_2/CO_2 ratio and is in the kinetic range (Ca less than 0.05) as H_2/CO_2 ratio increases from 3 to 7.

3.5. *Effect of co-feeding methane*

Co-feeding methane has a negligible effect on the rates or concentration gradient of the rate of formation or consumption of species in the channel reactor (Fig. 9a-c). The flow field remains laminar. There is negligible influence of methane on the concentration profiles of carbon dioxide, hydrogen, water, and carbon monoxide. Indeed, for carbon monoxide, there are no changes in concentration profiles upstream of the reactor (Fig. 9d). The concentration profiles of carbon monoxide show a maximum which stays constant with an increase in co-fed methane. As expected, methane does not affect the equilibrium of the reverse water gas shift reaction. The concentration gradients do not change with increasing co-feed of methane. Indeed, the changes to the concentration gradients are highest within 10% of the channel entry i.e., $x/L = 0.085$. Although methane has no effect on the conversion of carbon dioxide in the channel reactor, methane selectivity portrays a u-shaped behaviour with lowest selectivity at small amounts of co-fed methane (section S3 in supplementary information). At the same conversion, the carbon monoxide yield reduces with an increase in co-fed methane (Fig. 9e). While rates of reactant consumption i.e., carbon dioxide, and hydrogen reduce as channel length increases, rates of product i.e., methane, water, and carbon monoxide formation decrease as channel length increases.

The rates of carbon dioxide consumption do not change with a co-feed of methane and reduces with channel length. However, convection reduces with increasing amount of co-fed methane and increases with channel length. This leads to the highest Carberry numbers upstream of the channel reactor (Fig. 9f). The rate of carbon monoxide production is positive upstream of the channel reactor and negative downstream of the channel reactor.

3.6. *Effect of co-feeding steam*

Steam inhibits carbon dioxide methanation in the channel reactor (Fig. 10a). This inhibition effect has also been observed by Dittmeyer and co-workers (Farsi, 2020) over a micro-structured packed bed reactor with an internal cross-flow cooling channel and a milli-fixed bed reactor (Zhang et al., 2013). This has been attributed to the competitive adsorption of carbon dioxide and water on the active sites of the Ni/Al_2O_3 catalysts (Farsi, 2020). This could also be a thermodynamic effect attributed to the carbon dioxide methanation and reverse water gas shift reactions. As the amount of co-fed steam is increased, the conversion of carbon dioxide reduces. The gradients in the conversion of carbon dioxide reduces with an increase in co-fed steam (Fig. 10b and Fig. 10c). The biggest change in the gradient occurs within 10% of the channel entry. The rates of consumption of carbon dioxide, and hydrogen and the rates of formation of methane, water and carbon monoxide reduce with channel length and co-fed steam. The inhibition of steam on the rates of carbon dioxide methanation occurs downstream of the channel reactor. Conversely, changes in the concentration profiles of methane, carbon dioxide, and hydrogen occur downstream of the channel reactor (Figure S4 in supplementary information).

The yield of carbon monoxide exhibits a maximum with carbon dioxide conversion. The changes in carbon monoxide yield (Fig. 10d) occur downstream of the channel reactor with the maximum carbon monoxide yield occurring with lower quantities of co-fed steam (7.5%). The methane yield increases linearly with conversion with a maximum of ~ 50% yield (Fig. 10e).

Rates of carbon dioxide conversion is highest at the channel entry but decreases with an increase in co-fed steam and with channel length (Fig. 10f). The convective effects are highest at the channel exit. The

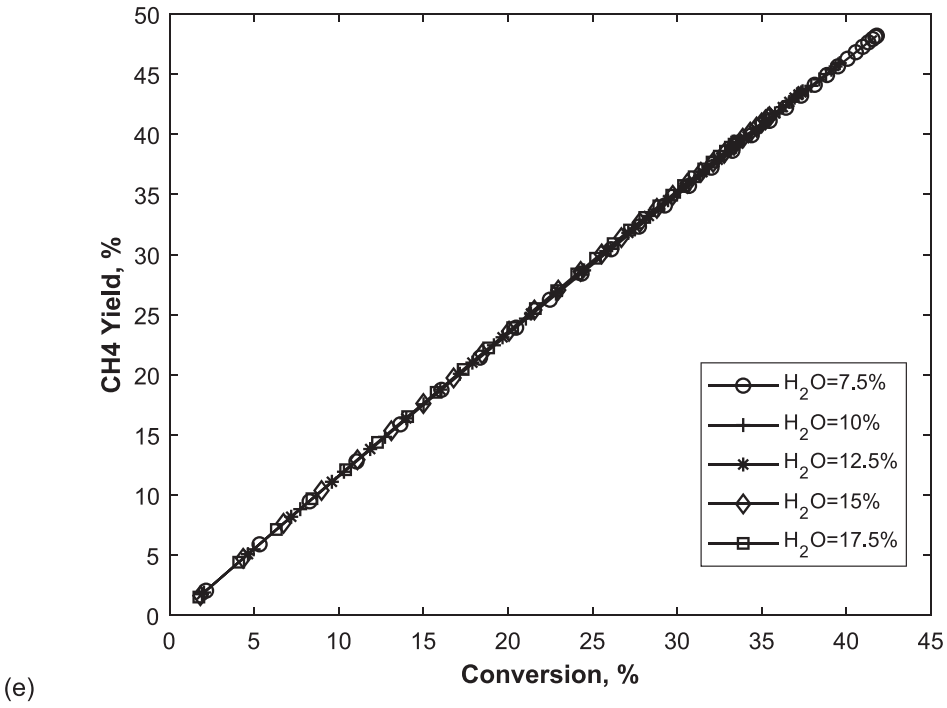

(e)

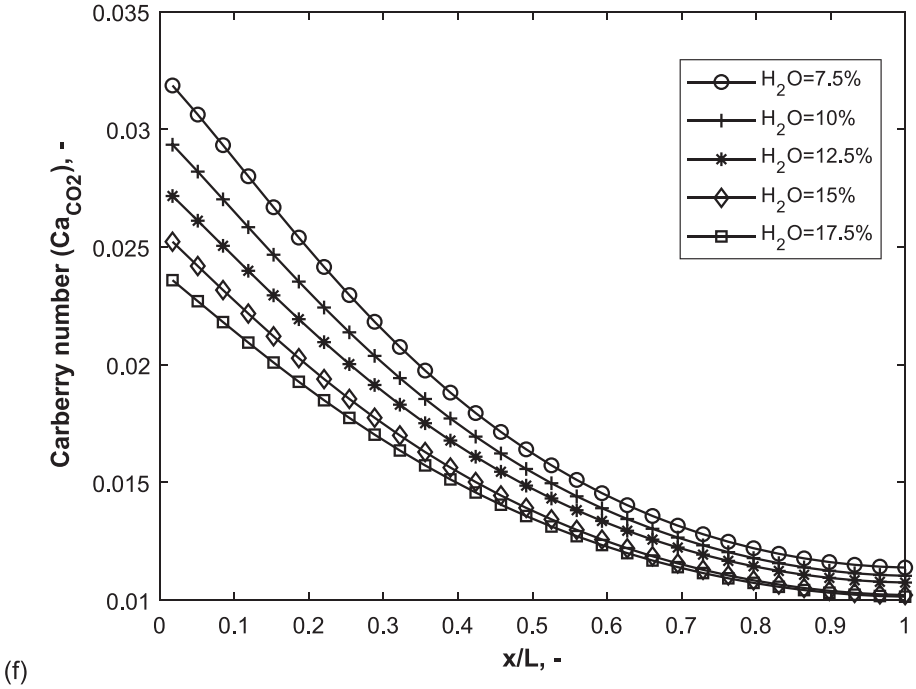

(f)

Fig. 10. (*continued*).

Carberry number, which gives a ratio of intrinsic kinetics to convective effects show that convection is not limiting during studies of the influence of co-fed steam.

3.7. Influence of pressure

Conversion increases with an increase in pressure (Fig. 11a). Kolb and co-workers observed an increase in reactor performance with pressure (Lefebvre et al., 2015). The concentration gradients across the channel length increase with an increase in pressure with most of the changes in gradients occurring upstream of the channel reactor (Fig. 11b and c). A maximum in carbon monoxide yield is obtained at about 30% conversion. The maximum in carbon monoxide yield reduces with an increase in pressure. At 1.2 bar, a maximum of 50% conversion is obtained (Fig. 11a). In fact, most of the changes in gradients occur within 10% of the channel length i.e., at about x/L = 0.083. A methane yield of 90% is reached at a conversion of 80%.

At 1.2 bar and 400 °C, the maximum Carberry number occurs at the channel entry. The maximum in Carberry number occurs because rates of carbon dioxide consumption decrease with pressure (Fig. 11b) and with axial length, and the diffusivities decrease with pressure while concentrations increase with pressure. This maximum in Carberry

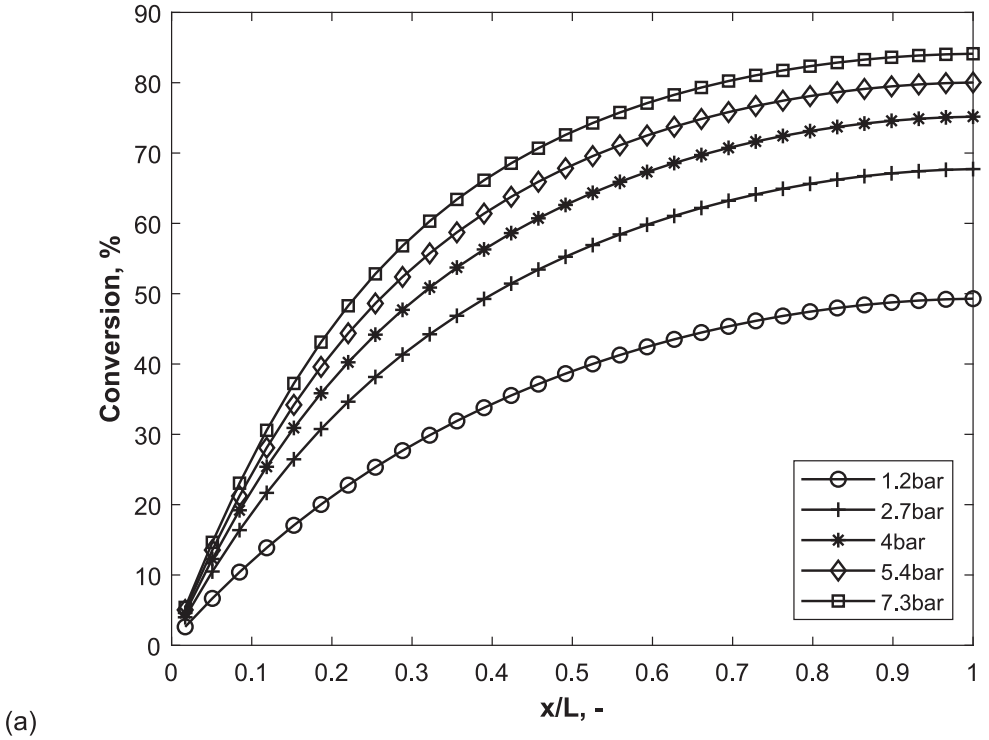

(a)

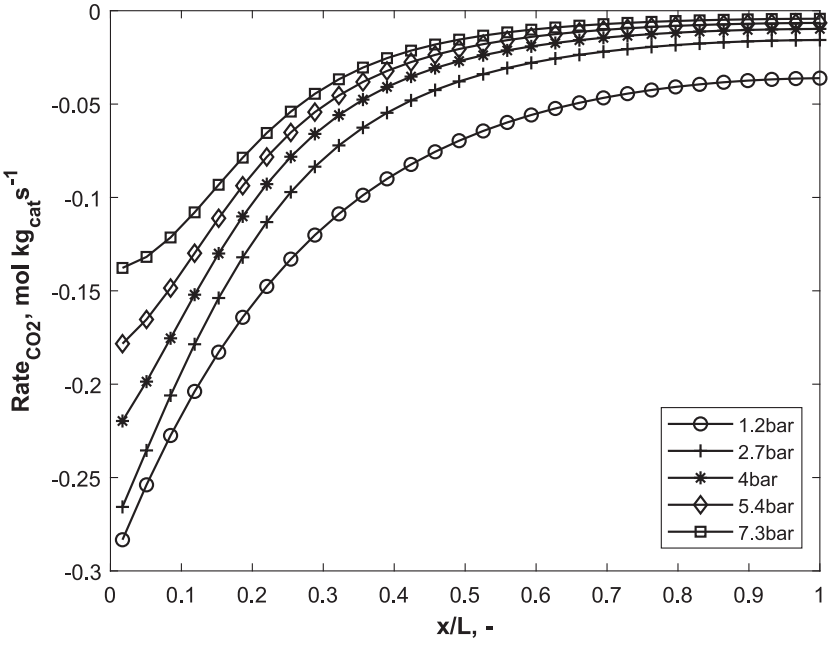

(b)

Fig. 11. (a) Conversion (b) CO_2 composition (c) concentration gradient (d) CO yield (e) CH_4 yield-conversion and (f) Carberry numbers obtained at 400 °C, 100 NmL min^{-1} and pressures ranging from 1.2 bar to 7.3 bar in the spatially resolved channel reactor.

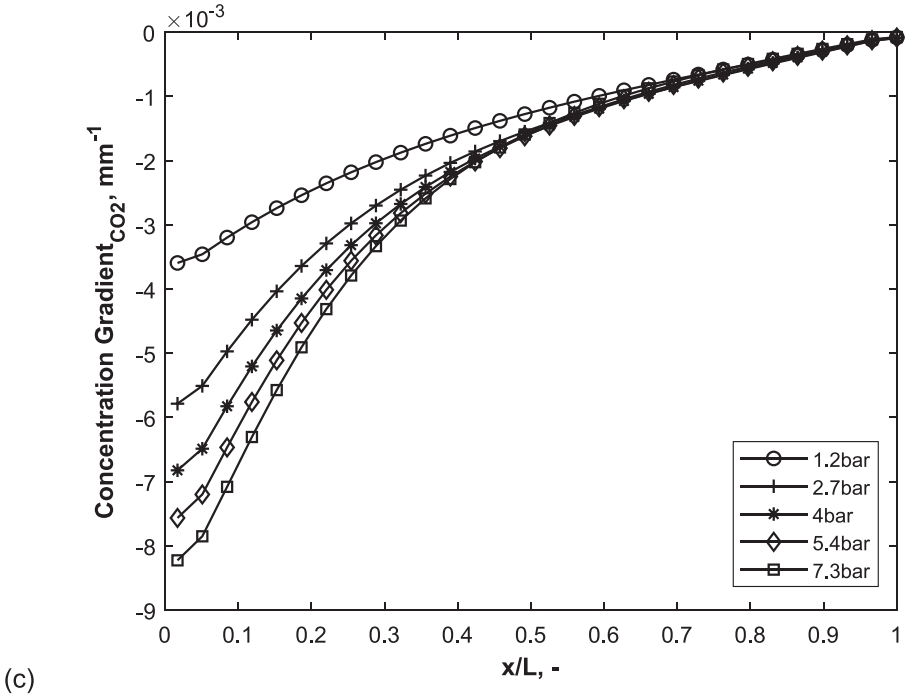

(c)

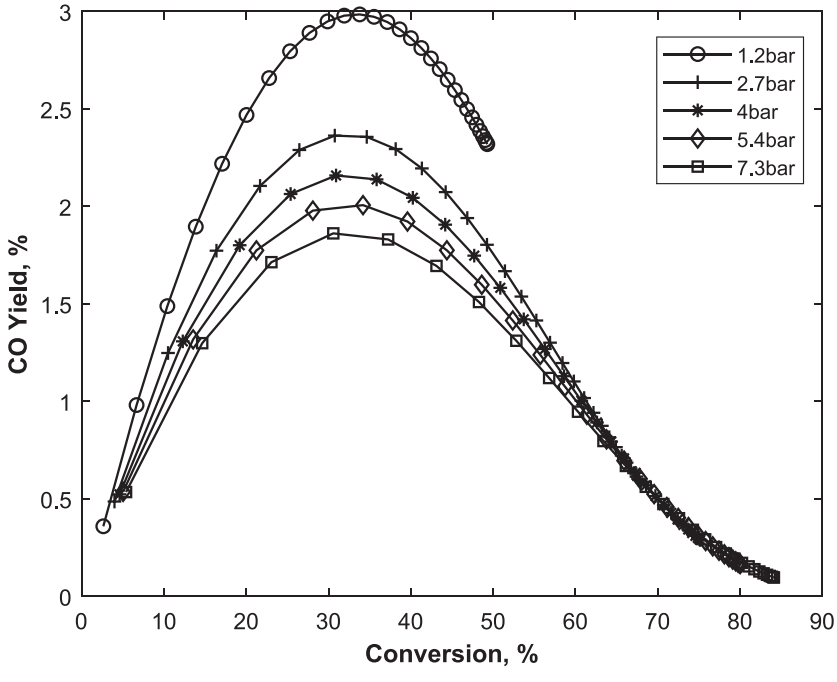

(d)

Fig. 11. (*continued*).

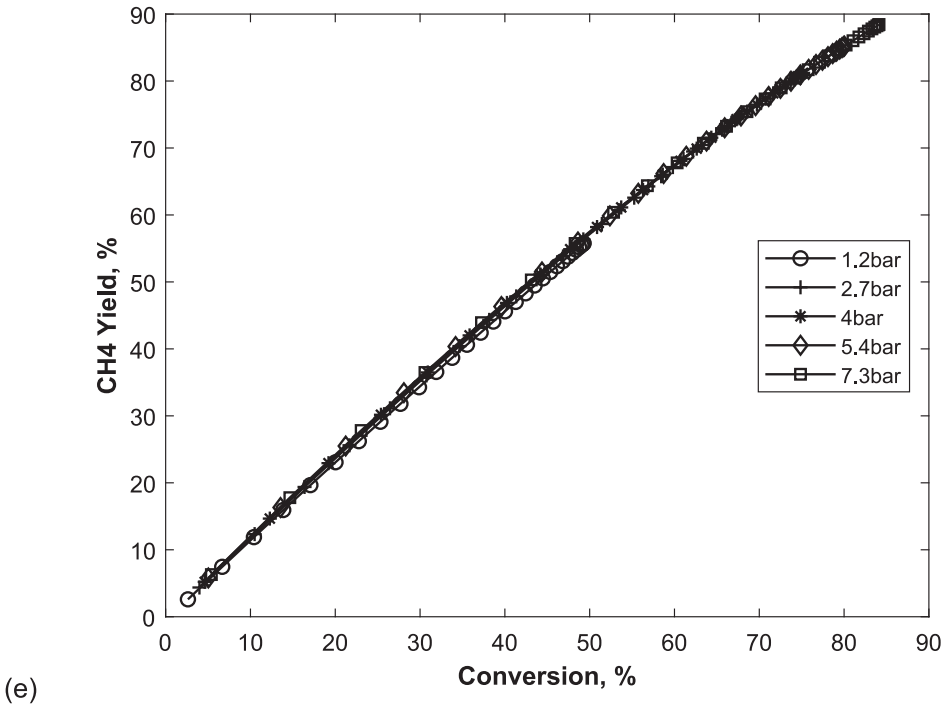

(e)

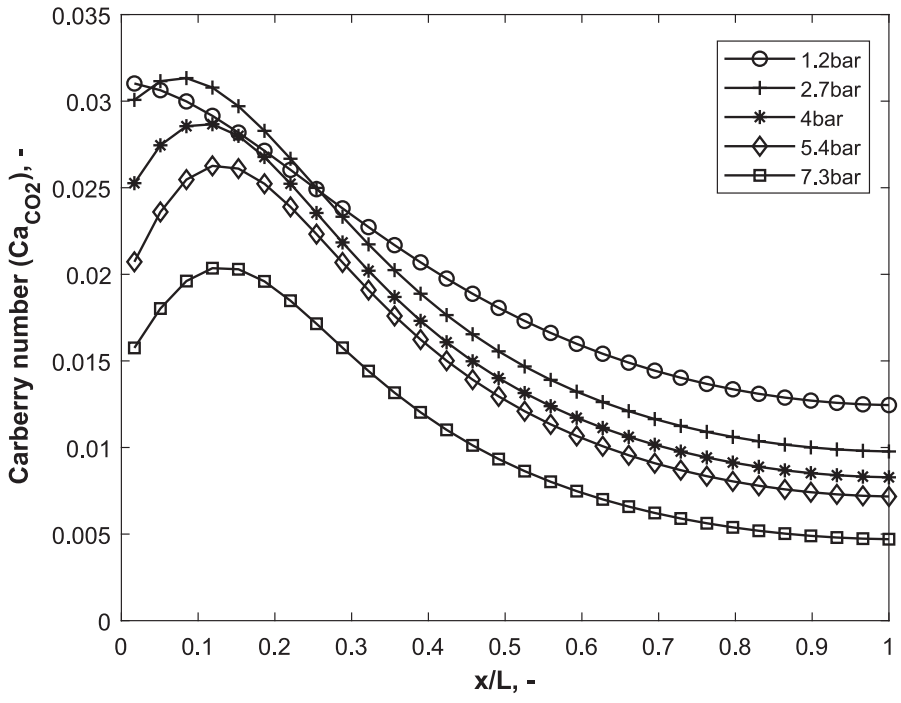

(f)

Fig. 11. (*continued*).

number moves further downstream as pressure is increased indicating more kinetic control. Maximum reaction rates occur at the reactor entry while convective effects are maximised at the channel exit.

3.8. Influence of temperature

The conversion increases with channel length and with temperature (Fig. 12a). Similar effects were observed for a slurry bubble column reactor during carbon dioxide methanation (Lefebvre et al., 2015). Carbon monoxide composition increases with axial length of the channel reactor up to 613 K. Thereafter, carbon monoxide composition depicts an overshoot profile with channel length. The amount of carbon monoxide released increases with temperature (Fig. 12b). Likewise, the yield in carbon monoxide is linear with conversion up to a temperature of 613 K. Thereafter, the yield of carbon monoxide exhibits a maximum at higher temperatures (Fig. 12c). The studies carried out in sections 3.3 to 3.8 were conducted at 400 °C. In sections 3.3 and 3.9, we observe that the change in shape from linear to a maximum in carbon monoxide yield with conversion occurs with an increase in temperature. This is due to the competition between the water gas shift reaction and the reverse water gas shift reaction with temperature. The water gas shift reaction is activated at higher temperatures. The change in molar composition, that

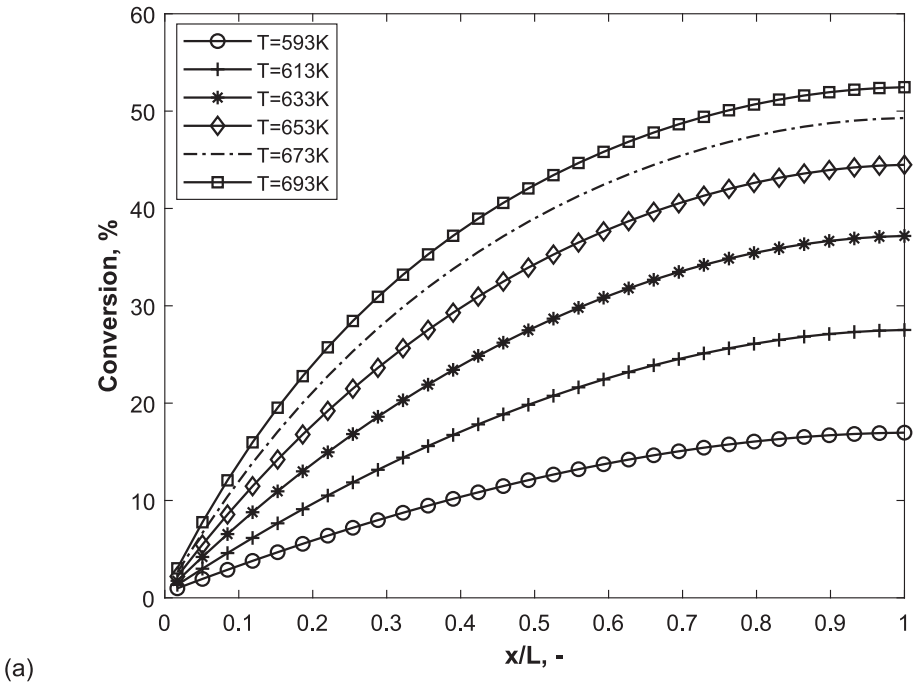

(a)

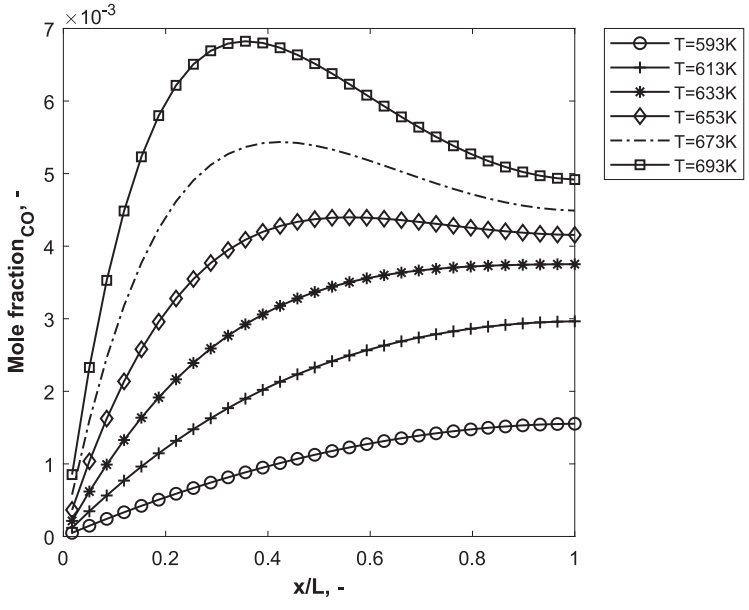

(b)

Fig. 12. (a) Conversion (b) CO composition (c) CO yield-conversion (d) CH_4 yield-conversion (e) CO_2 rate gradient (f) Carberry number determined at 1.2 bar, 100 NmL min^{-1} and temperatures between 320 °C and 420 °C in the spatially resolved channel reactor at a constant H_2/CO_2 ratio of 4.

results from an activation of the water gas shift reaction at higher temperatures, results in the maximum in the yield of carbon monoxide with temperature above 380 °C.

The yield of methane is linear with conversion (Fig. 12d). In conventional reactors, external mass and heat transfer influences are usually determined at the reactor exit. The Carberry number is less than 0.5 for all simulations for variations in temperatures showing kinetic regime. Maximum reaction rates occur at the reactor entry while convective effects are maximised at the channel exit. At low temperatures, rates balance out convective effects. With increasing temperatures, rates are highest at the channel entry while convective effects are highest at the channel exit. The rates have a higher influence over convective effects and convective effects are non-limiting.

Interestingly, we observe that differential rates (Fig. 12e) in carbon dioxide consumption can be obtained at conversions up to 30% in the channel reactor. Differential rates during kinetic studies occur in two scenarios namely: (a) at less than 5% conversion in fixed bed reactors: this can be observed also in channel reactors (Fig. 6c), (b) at higher conversions in a continuous stirred-tank reactor such as the Berty reactor (Sughrue and Bartholomew, 1982; Pille et al., 1994). We observe that mass transport limitations are attenuated close to the channel entry for conversions less than 30% (Fig. 12f). At low temperatures, we observe that the rates of carbon dioxide conversion (R_{CO2}) have a relatively negligible dependence on the mole fraction of carbon dioxide

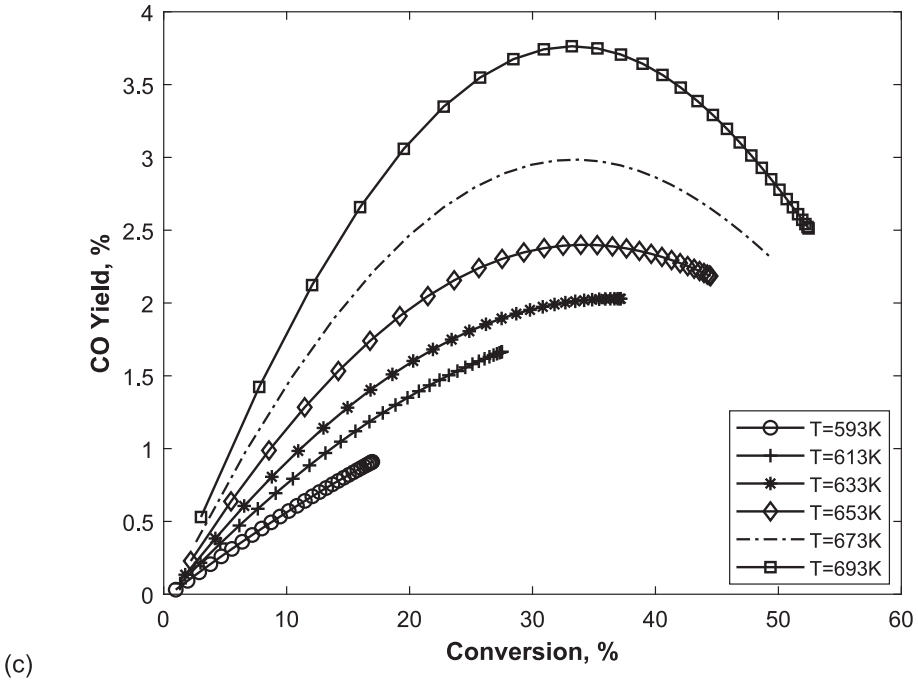

(c)

Fig. 12. (*continued*).

(Fig. 13) for conversions less than 30%. While the conversion changes up to 30%, there is negligible change in the rates of carbon dioxide conversion at low temperatures leading to differential rates. This is implicit in the nature of the LHHW kinetic model.

As the rates of methanation (r_1) and RWGS (r_2) are each a function of (equation (12)): driving force and rate constant, equilibrium term, adsorption term, further investigations were carried out to obtain which term leads to differential rates at 30% conversion. It is important to note that the rate of carbon dioxide conversion is equal to the sum of the rates of methanation and RWGS i.e., $R_{CO2} = -r_1 - r_2$. We observe that the equilibrium term of the reverse water gas shift reaction, that is $1 - \left(K_\beta \frac{p_{CO} \bullet p_{H2O}}{p_{H2} \bullet p_{CO2} \bullet K_{eqRWGS}}\right)$, plays the key role in determining differential rates of carbon dioxide conversion (Fig. 14).

3.9. Relevance of spatially resolved channel plate reactor studies

Kinetic experiments and modelling of carbon dioxide methanation which are based on "end-of-pipe" measurements will not reveal the maximum in carbon monoxide concentration profiles that are observed with an increase in temperature, pressure, H_2/CO_2 ratio, flowrate and with co-fed steam, and co-fed methane. The kinetic models derived based on "end-of-pipe" measurements may be erroneous. Spatially resolved measurements allow for full elucidation of the kinetic profiles and the fitting of experimental data to model along the channel reactor provides greater precision for kinetic modelling studies and reactor design.

At high conversions, integral rates are obtained, and concentration and temperature gradients ensue. These gradients can be uniform or non-uniform. We observe that these gradients vary both along the axial length of the channel reactor and the channel depth. The nature of the gradients in gas composition or rates of carbon dioxide conversion changes depending on the process conditions. We observe uniform gradients for flowrates at low temperatures, but non-uniform gradients at high temperatures. We observe uniform gradients with H_2/CO_2, co-fed steam, co-fed methane and with pressure and a switch from uniform gradients at low temperatures to non-uniform gradients at high temperatures. Characterisation of these gradients shows where the regions of highest mass transfer occur along the length of the channel reactor. Spatially resolved studies allow for gradient characterisation.

Differential rates are usually obtained at low conversions. This can be found where the rate is expressed as a simple power law expression of concentration. Overall, we observe that at relatively high conversions, differential rates could still be obtained due to the intricate nature of the LHHW kinetic model. Although the LHHW model gives the best agreement with experimental data by Kopyscinski and co-workers based on DRIFTS spectroscopy and spatially resolved channel reactor studies, this model is insensitive to the gas composition of carbon dioxide along the channel length of the reactor at low temperatures. This is because the rate of the reverse water gas shift reaction, r_2, has a negligible dependence on the mole fraction of carbon dioxide at low temperatures. Consequently, at low temperatures, we obtain differential rates at relatively high conversions.

The spatially resolved studies reveal highest rates of carbon dioxide conversion at the channel entry and highest rates of convection at the channel exit. Overall mass transport is limiting at the reactor entry. This results in a high Carberry number at the reactor entry, which decreases with channel length. However, mass transfer control is usually determined at the reactor exit of the channel reactor. We observe a decrease of Carberry number with channel length at low pressures and as pressure is increased, the Carberry number goes through a maximum before decreasing. Such nuanced effects of the switch between kinetic control and mass transfer control can only be revealed through a spatially resolved channel reactor study. This behaviour is observed with a methane co-feed. Due to the aforementioned studies, a combined approach of spatially resolved experiments and $2D_{x\text{-}z}$ simulations of channel reactors is very important.

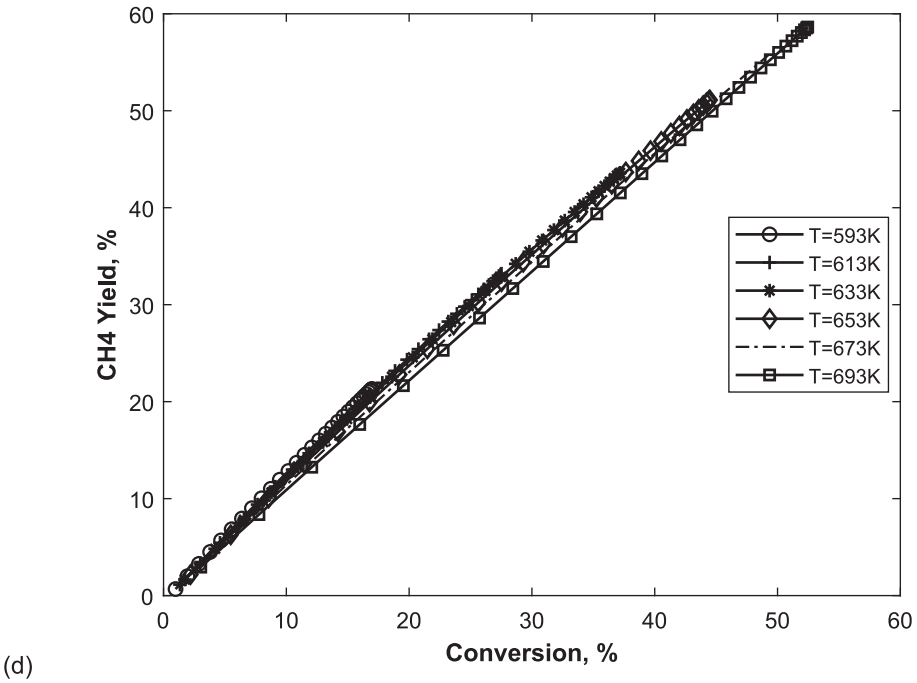

(d)

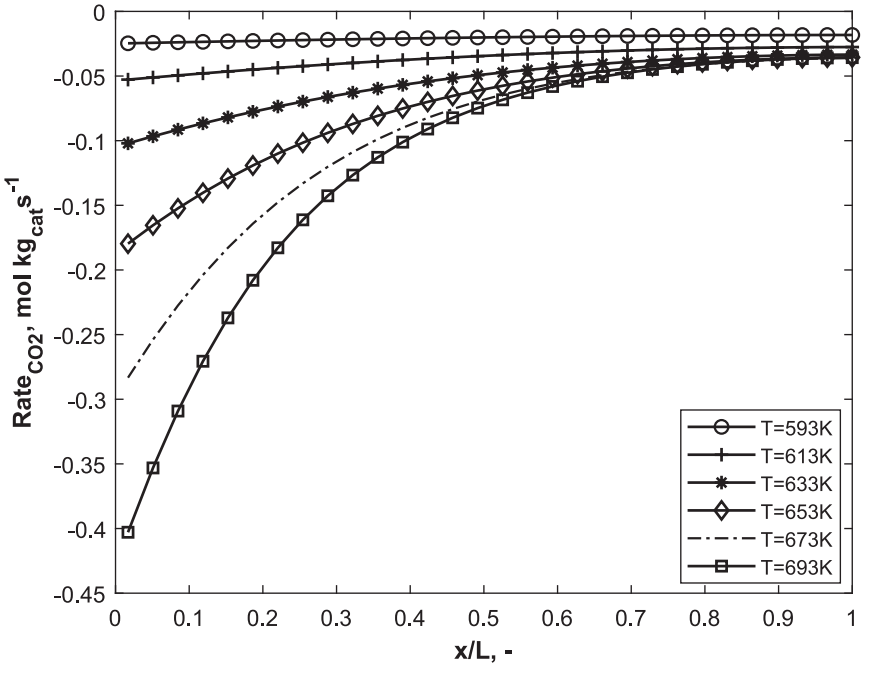

(e)

Fig. 12. (*continued*).

4. Conclusions

Carbon dioxide methanation has been studied in a channel plate reactor with different co-feeds (methane, and steam), at different flowrates, at various H_2/CO_2 ratios and with increasing pressure and temperature. Various reactor (1D, $2D_{x\text{-}z}$) models were compared using parameters derived based on a kinetic model obtained from spatially resolved channel reactor experiments and DRIFTS spectroscopy. The $2D_{x\text{-}z}$ pseudo-homogeneous CFD model gives good agreement with experimental data and compares favourably with the 1D model. Latitudinal changes are also observed in the species concentration in a $2D_{x\text{-}z}$ model, which are attenuated towards the reactor exit and strengthened with flowrate, in agreement with experimental data. Methane yield increases linearly with conversion. The yield of carbon monoxide is linear with conversion at low temperatures. At higher temperatures, and with increasing H_2/CO_2 ratios, with a co-feed of methane and steam and with increasing pressure, carbon monoxide yield displays a maximum with conversion. Methane does not inhibit carbon dioxide conversion while co-feeding steam reduces the reactor performance. Rate and concentration gradients are highest at the channel reactor entry and maximum changes in concentration and rate gradients occur within 10% of the channel entry. At low temperatures with a conversion of up to 30%,

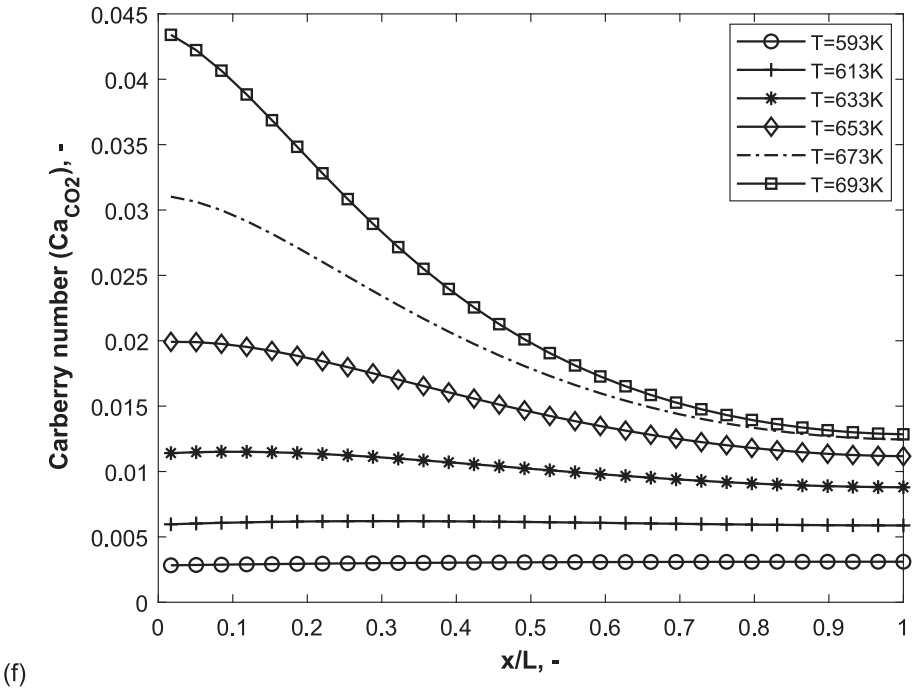

(f)

Fig. 12. (*continued*).

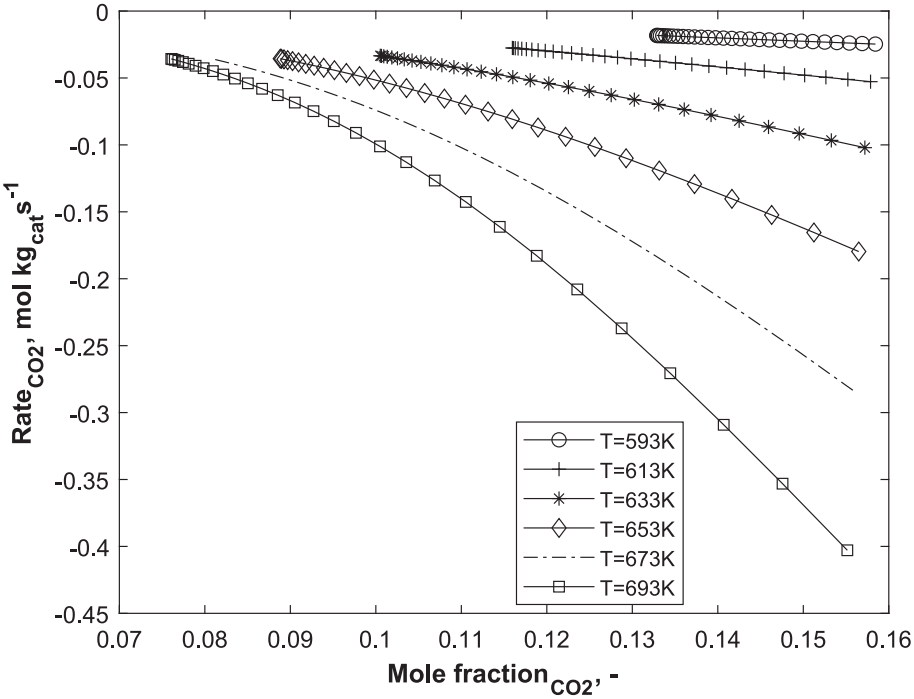

Fig. 13. Dependence of mole fraction of carbon dioxide on the rates of carbon dioxide conversion between 320 °C and 420 °C at 1.2 bar, 100 NmL min^{-1} in the spatially resolved channel reactor at a constant H_2/CO_2 ratio of 4.

differential rates are obtained. This is due to negligible dependence of the rate of carbon dioxide conversion on the gas composition on carbon dioxide at low temperatures. Specifically, the equilibrium term of the reverse water gas shift reaction has a negligible dependence on the mole fraction of carbon dioxide along the channel length at low temperatures. These results are relevant to the design of channel reactors for kinetic analysis and for improving the performance of carbon dioxide methanation for power-to-gas applications.

Declaration of Competing Interest

The authors declare that they have no known competing financial interests or personal relationships that could have appeared to influence the work reported in this paper.

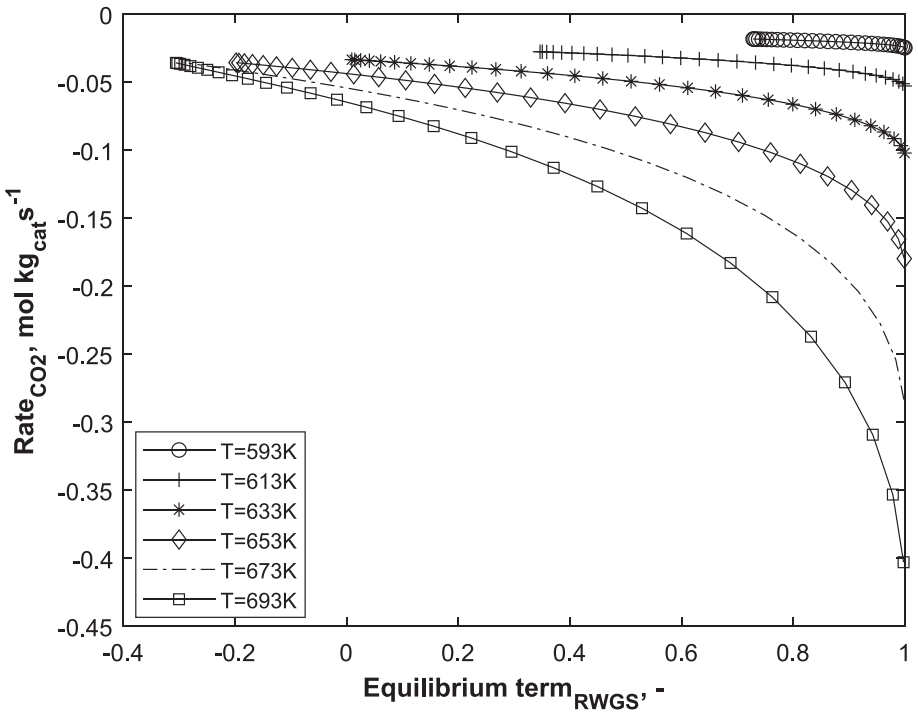

Fig. 14. A plot of the rates of carbon dioxide conversion with the equilibrium term of the reverse water gas shift reaction.

Data availability

All validation data used in this work were obtained from archived literature. Research code can be found at https://www.tfd.chalmers.se/~lada/pyCALC-RANS.html.

Acknowledgements

Funding from the Chalmers Area of Advance Transport is gratefully acknowledged. The presented work contributes to the competence centre TechForH2. TechForH2 is hosted by Chalmers University of Technology and is financially supported by the Swedish Energy Agency (P2021-90268) and the member companies Volvo, Scania, Siemens Energy, GKN Aerospace, PowerCell, Oxeon, RISE, Stena Rederier AB, Johnson Matthey and Insplorion.

Appendix A. Supplementary data

Supplementary data to this article can be found online at https://doi.org/10.1016/j.ces.2023.119235.

References

Alarcón, A., Guilera, J., Andreu, T., 2021. An insight into the heat-management for the CO2 methanation based on free convection. Fuel Process. Technol. 213, 106666.
Bengaouer, A., Ducamp, J., Champon, I., Try, R., 2018. Performance evaluation of fixed-bed, millistructured, and metallic foam reactor channels for CO2 methanation. Can. J. Chem. Eng. 96 (9), 1937–1945.
Bird, B.R., W.E. Stewart, and E.N. Lightfoot, Transport Phenomena Revised 2nd ed. 2007: John Wiley & Sons, Inc.
Bosco, M., Vogel, F., 2006. Optically accessible channel reactor for the kinetic investigation of hydrocarbon reforming reactions. Catal. Today 116 (3), 348–353.
Burger, T., Donaubauer, P., Hinrichsen, O., 2021. On the kinetics of the co-methanation of CO and CO2 on a co-precipitated Ni-Al catalyst. Appl. Catal. B 282, 119408.
Chandraker, V., Paramasivan, G., Chandy, A.J., 2022. Computational investigations of enrichment effects for CO2 methanation in Sabatier microchannel reactors. Chem. Eng. Res. Des. 182, 51–65.
Chiang, J.H., Hopper, J.R., 1983. Kinetics of the hydrogenation of carbon dioxide over supported nickel. Ind. Eng. Chem. Prod. Res. Dev. 22 (2), 225–228.
Danilov, V.A., Wichert, M., Kolb, G., 2022. 2D model of the transfer processes for CO2 methanation in a microchannel reactor. Chem. Eng. J. 450, 137863.
Davidson, L., A Python Code for Two-Dimensional Turbulent Steady Flow. 2021.
Engelbrecht, N., Chiuta, S., Everson, R.C., Neomagus, H.W.J.P., Bessarabov, D.G., 2017. Experimentation and CFD modelling of a microchannel reactor for carbon dioxide methanation. Chem. Eng. J. 313, 847–857.
Engelbrecht, N., Everson, R.C., Bessarabov, D., 2020. Thermal management and methanation performance of a microchannel-based Sabatier reactor/heat exchanger utilising renewable hydrogen. Fuel Process. Technol. 208, 106508.
European-Commission, Proposal for a directive of the european parliament and of the council. 2021, European Commission: Brussels.
Fache, A., Marias, F., 2020. Dynamic operation of fixed-bed methanation reactors: yield control by catalyst dilution profile and magnetic induction. Renew. Energy 151, 865–886.
Falbo, L., Martinelli, M., Visconti, C.G., Lietti, L., Bassano, C., Deiana, P., 2018. Kinetics of CO2 methanation on a Ru-based catalyst at process conditions relevant for Power-to-Gas applications. Appl. Catal. B 225, 354–363.
Farsi, S., et al., 2020. A consecutive methanation scheme for conversion of CO2 – A study on Ni3Fe catalyst in a short-contact time micro packed bed reactor. Chem. Eng. J. 388, 124233.
Farsi, S., Liang, S., Pfeifer, P., Dittmeyer, R., 2021. Application of evaporation cooling in a microstructured packed bed reactor for decentralized CO2 methanation. Int. J. Hydrogen Energy 46 (38), 19971–19987.
Froment, G.F., K.B. Bischoff, and J. De Wilde, Chemical Reactor Analysis and Design. 3rd Edition ed. 2011: John Wiley & Sons.
Garbarino, G., Pugliese, F., Cavattoni, T., Busca, G., Costamagna, P., 2020. A study on CO2 methanation and steam methane reforming over commercial Ni/calcium aluminate catalysts. Energies 13 (11), 2792.
Garbis, P., Kern, C., Jess, A., 2019. Kinetics and reactor design aspects of selective methanation of CO over a Ru/γ-Al 2 O 3 catalyst in CO 2 /H 2 rich gases †. Energies 12 (3), 469.
Götz, M., Lefebvre, J., Mörs, F., McDaniel Koch, A., Graf, F., Bajohr, S., Reimert, R., Kolb, T., 2016. Renewable power-to-gas: a technological and economic review. Renew. Energy 85, 1371–1390.
Hernandez Lalinde, J.A., et al., 2020. CO2 methanation and reverse water gas shift reaction. Kinetic study based on in situ spatially-resolved measurements. Chem. Eng. J. 390, 124629.
Hernandez Lalinde, J.A., Kofler, K., Huang, X., Kopyscinski, J., 2018. kinetic data acquisition using an optically accessible catalytic plate reactor with spatially-resolved measurement techniques case of study: CO2 methanation. Catalysts 8 (2), 86.
Inoue, H., Funakoshi, M., 1984. Kinetics of methanation of carbon monoxide and carbon dioxide. J. Chem. Eng. Jpn. 17 (6), 602–610.
Kai, T., Takahashi, T., Furusaki, S., 1988. Kinetics of the methanation of carbon dioxide over a supported Ni-La2O3 catalyst. Can. J. Chem. Eng. 66 (2), 343–347.
Kopyscinski, J., Schildhauer, T.J., Vogel, F., Biollaz, S.M.A., Wokaun, A., 2010. Applying spatially resolved concentration and temperature measurements in a catalytic plate reactor for the kinetic study of CO methanation. J. Catal. 271 (2), 262–279.
Lalinde, J.A.H., Jiang, J., Jai, G., Kopyscinski, J., 2019. Preparation and characterization of Ni/Al2O3 catalyst coatings on FeCrAl-loy plates used in a catalytic channel reactor with in-situ spatial profiling to study CO2 methanation. Chem. Eng. J. 357, 435–446.

Lefebvre, J., Götz, M., Bajohr, S., Reimert, R., Kolb, T., 2015. Improvement of three-phase methanation reactor performance for steady-state and transient operation. Fuel Process. Technol. 132, 83–90.
Miguel, C.V., Mendes, A., Madeira, L.M., 2018. Intrinsic kinetics of CO2 methanation over an industrial nickel-based catalyst. J. CO2 Util. 25, 128–136.
Ngo, S.I., et al., 2020. Flow behaviors, reaction kinetics, and optimal design of fixed- and fluidized-beds for CO2 methanation. Fuel 275, 117886.
Pérez, S., Del Molino, E., Barrio, V.L., 2019. Modeling and Testing of a Milli-Structured Reactor for Carbon Dioxide Methanation. 17, 11.
Pille, R.C., Yu, C.-y., Froment, G.F., 1994. Kinetic study of the hydrogen sulfide effect in the conversion of thiophene on supported CoMo catalysts. J. Mol. Catal. 94 (3), 369–387.
Raghu, A.K., Kaisare, N.S., 2019. Analysis of the autothermal operability of the Sabatier reaction in a heat-recirculating microreactor using CFD. React. Chem. Eng. 4 (10), 1823–1833.
Raghu, A.K., Kaisare, N.S., 2022. Thermally integrated microreactor for Sabatier reaction: study of air-cooled and inert-diluted counter-current operation strategies. Catal. Today 383, 146–155.
Raja, L.L., Kee, R.J., Deutschmann, O., Warnatz, J., D. Schmidt, L., 2000. A critical evaluation of Navier-Stokes, boundary-layer, and plug-flow models of the flow and chemistry in a catalytic-combustion monolith. Catal. Today 59 (1-2), 47–60.
Schlereth, D., Donaubauer, P.J., Hinrichsen, O., 2015. Metallic honeycombs as catalyst supports for methanation of carbon dioxide. Chem. Eng. Technol. 38 (10), 1845–1852.
Schmider, D., Maier, L., Deutschmann, O., 2021. Reaction kinetics of CO and CO2 methanation over nickel. Ind. Eng. Chem. Res. 60 (16), 5792–5805.
Serrer, M.-A., Stehle, M., Schulte, M.L., Besser, H., Pfleging, W., Saraçi, E., Grunwaldt, J.-D., 2021. Spatially-resolved insights into local activity and structure of Ni-based CO2 methanation catalysts in fixed-bed reactors. ChemCatChem 13 (13), 3010–3020.
Sughrue, E.L., Bartholomew, C.H., 1982. Kinetics of carbon monoxide methanation on nickel monolithic catalysts. Appl. Catal. 2 (4), 239–256.
Sun, D., Khan, F.M., Simakov, D.S.A., 2017. Heat removal and catalyst deactivation in a Sabatier reactor for chemical fixation of CO2: Simulation-based analysis. Chem. Eng. J. 329, 165–177.
Surendran, V., et al., 2022. Assessment of a catalytic plate reactor with in-situ sampling capabilities by means of CFD modeling and experiments. Chem. Eng. J. 446, 136999.
Türks, D., Mena, H., Armbruster, U., Martin, A., 2017. Methanation of CO2 on Ni/Al2O3 in a structured fixed-bed reactor—a scale-up study. Catalysts 7 (5), 152.
Van Herwijnen, T., Van Doesburg, H., De Jong, W.A., 1973. Kinetics of the methanation of CO and CO2 on a nickel catalyst. J. Catal. 28 (3), 391–402.
Vidal Vázquez, F., Kihlman, J., Mylvaganam, A., Simell, P., Koskinen-Soivi, M.-L., Alopaeus, V., 2018. Modeling of nickel-based hydrotalcite catalyst coated on heat exchanger reactors for CO2 methanation. Chem. Eng. J. 349, 694–707.
Weatherbee, G.D., Bartholomew, C.H., 1981. Hydrogenation of CO2 on group VIII metals: I. Specific activity of NiSiO2. J. Catal. 68 (1), 67–76.
Weatherbee, G.D., Bartholomew, C.H., 1982. Hydrogenation of CO2 on group VIII metals: II. Kinetics and mechanism of CO2 hydrogenation on nickel. J. Catal. 77 (2), 460–472.
Wulf, C., Linßen, J., Zapp, P., 2018. Review of power-to-gas projects in Europe. Energy Procedia 155, 367–378.
Zhang, J., Fatah, N., Capela, S., Kara, Y., Guerrini, O., Khodakov, A.Y., 2013. Kinetic investigation of carbon monoxide hydrogenation under realistic conditions of methanation of biomass derived syngas. Fuel 111, 845–854.